Aus der Klinik für Radiologie

der Medizinischen Fakultät Charité – Universitätsmedizin Berlin

DISSERTATION

Quantitative tissue characterization by mechanical parameters in preclinical, small-animal models

Quantitative Gewebecharakterisierung mittels mechanischer Kenngrößen in präklinischen Kleintiermodellen

zur Erlangung des akademischen Grades

Doctor of Philosophy (PhD)

vorgelegt der Medizinischen Fakultät

Charité – Universitätsmedizin Berlin

von

Gergely Bertalan

aus Nové Zámky, die Slowakei

Datum der Promotion: 18.09.2020

Table of Contents

List of Abbreviations

0.5-T	0.5 Tesla
7-T	7 Tesla
3D	Three-dimensional
ADC	Apparent diffusion coefficient
AHI	Algebraic Helmholtz inversion
ASL	Arterial spin labeling
B_0	Static magnetic field of the scanner
CA	Cardiac arrest
CBF	Cerebral blood flow
CC	Corpus callosum
CO	Cortex
CW	Cranial window
DWI	Diffusion weighted imaging
DI	Diencephalon
EPI	Spin-echo echo-planar imaging
FLASH	Fast low angle shot
GM	Grey matter
HAI	Hypoxic-anoxic injury
HP	Hippocampus
k-MDEV	*k*-based multifrequency-dual elasto-visco inversion
LFE	Local frequency estimation
MR	Magnetic resonance
MDEV	Elasto-visco inversion
MEG	Motion encoding gradient
MRE	Magnetic resonance elastography
MRS	Magnetic resonance spectroscopy
PM	*post mortem*

RA	Respiratory arrest
ROI	Region of interest
SNR	Signal to noise ratio
SLIM	Sample interval modulation
SWS	Shear wave speed
TE	Echo time
TR	Repetition time
WB	Whole brain
WM	White matter

List of Figures

List of Tables

Zusammenfassung

Die biomechanischen Eigenschaften von zerebralem Gewebe beeinflussen zahlreiche physiologische Prozesse im Gehirn. Die zerebrale Magnetresonanz-Elastographie (MRE) erwies sich dabei innerhalb des letzten Jahrzehnts als wertvolles nicht-invasives Bildgebungsverfahren und offenbarte wichtige biomechanische Merkmale im gesunden als auch kranken Gewebe. Die moderne MRE des Maushirns ist jedoch durch zeitaufwändige Multi-Shot-Bildaufnahemetechniken und rauschempfindliche monofrequente Bildrekonstruktionsmethoden begrenzt. Das Ziel dieser Promotion war die Entwicklung eines hochauflösenden Elastographie-Verfahrens mittels multifrequenter Maushirn-MRE auf der Grundlage von Einzelbildaufnahmetechniken und anschließender Tomoelastographie-Postprozessierung zur Minderung der Rauschempfindlichkeit.

Die Durchführbarkeit der Methode wurde mit drei *in-vivo*-Studien nachgewiesen. In der ersten Studie wurden verschiedene Bereiche des Gehirns bezüglich der Scherwellengeschwindigkeit (SWS) als Surrogat der Steifigkeit vermessen. Die zweite Studie untersuchte den Einfluss der Körpertemperatur auf biophysikalische Parameter des murinen Hirngewebes im normothermen bis hypothermen Bereich. Die Tomoelastographie wurde mit arterieller Spin-Markierung und diffusionsgewichteter Bildgebung kombiniert, um mögliche Zusammenhänge zwischen Gewebesteifigkeit, Perfusion und Diffusion zu analysieren. Im Rahmen der dritten Studie wurden anhand eines hypoxischen Mausmodells die biomechanischen Veränderungen des Gehirns während der kritischen Phase des Todes kontinuierlich aufgenommen und überwacht.

Für zehn Tiere wurden lokale SWS von 2,9 ± 0,2 m/s für das Corpus callosum, 4,9 ± 0,5 m/s für den Hippocampus, 4,8 ± 0,8 m/s für das Zwischenhirn und 3,5 ± 0,3 m/s für den Cortex cerebri quantifiziert. Anhand von sechs vermessenen Tieren konnte im gesamten Gehirn, Kortex und Hippocampus eine Abnahme der SWS von Hypo- (28 ± 0.5 °C) zu Normothermie (38 ± 0.5 °C) jeweils um 6,2%, 10,1% bzw. 7,4% festgestellt werden. Diese Abnahme der SWS korrelierte mit Veränderungen der Wasserdiffusion (30% Zunahme) und der Perfusion (60% bis 90% Zunahme). Darüber hinaus führte der Hirntod bei vierzehn Tieren zu einem Anstieg der SWS um 6% im gesamten Gehirn und 9% im Hippocampus gegenüber den in-vivo-Werten.

Das implementierte neuartige Multifrequenz-MRE-Verfahren liefert innerhalb stark verkürzter Messzeiten Steifigkeitskarten vom Maushirn mit größerer Detailauflösung als bisherige MRE Methoden. Erstmals konnten somit klinisch relevante biophysikalische Prozesse im Gehirn wie

die Hypothermie, die Hypoxie und die kritische Phase des Hirntodes beobachtet und untersucht werden. Die Ergebnisse zeigen, dass die Steifigkeit in den verschiedenen Subregionen des Gehirns der Maus variiert, mit der Wasserdiffusion und der Perfusion invers korreliert und durch Hypoxie im Rahmen des Hirntodes zunimmt. Die neuen Entwicklungen tragen zum wachsenden Verständnis der biomechanischen Eigenschaften des Hirngewebes bei.

Abstract

The biomechanical properties of the brain play an important role in vital functioning and disease development. Over the last decade, cerebral magnetic resonance elastography (MRE) has emerged as a valuable imaging technique, revealing important characteristics of tissue biomechanics in disease and health. However, state-of-the-art mouse brain MRE is limited by time-consuming multi-shot acquisition techniques and noise-sensitive single-frequency image reconstruction methods. Therefore, the purpose of this PhD project was the development of multifrequency mouse brain MRE based on a single-shot acquisition technique and noise-robust tomoelastography post-processing for high-resolution stiffness mapping.

The feasibility of the method was demonstrated using three *in vivo* studies. In the first study, shear wave speed (SWS) as a surrogate of stiffness in different areas of the brain was measured. In the second study, the effect of body temperature on biophysical parameters of murine brain tissue was investigated in the normothermic to hypothermic range. Tomoelastography was combined with arterial spin labelling and diffusion-weighted imaging in order to determine the relationship between tissue stiffness, perfusion and diffusion. In the third study, mechanical brain alterations were continuously monitored during the critical phase of death in a mouse model of hypoxia.

In ten animals, we quantified regional dependent SWS of 2.9 ± 0.2 m/s, 4.9 ± 0.5 m/s, 4.8 ± 0.8 m/s and 3.5 ± 0.3 m/s for the corpus callosum, hippocampus, diencephalon and cortex. In a group of six animals, we found that SWS decreased from hypothermia (28 ± 0.5 °C) to normothermia (38 ± 0.5 °C) by 6.2%, 10.1% and 7.4% in the whole brain, cortex and hippocampus, respectively. These SWS decreases were correlated with changes in water diffusion (30% increase) and blood perfusion (60% to 90% increase). Furthermore, in fourteen animals, brain death led to a 6% increase of SWS in the whole brain and 9% in the hippocampus when compared to *in vivo* values.

Our novel multifrequency MRE method with tomoelastography processing provides mouse brain stiffness maps within shorter scan times and with greater detail resolution than a conventional MRE. Short scan times, in the order of only 40 seconds, open new horizons for continuous stiffness monitoring during different pathological processes *in vivo*. Clinical relevant biophysical processes in the brain, such as hypothermia and hypoxia, and the critical phase of brain death were monitored and investigated for the first time. The results show that

stiffness varies across sub-regions in the murine brain, is inversely correlated with water diffusion and blood perfusion, and increases in hypoxia towards brain death. The new method contributes to the growing understanding of mechanical signatures of brain tissues and is potentially of great value for future studies of *in vivo* brain mechanical properties in health and disease.

1. Introduction

Studying the biomechanical properties of the brain adds new information to the understanding of brain functioning and disease development. Over the last decade, magnetic resonance elastography (MRE) has emerged as a valuable imaging method for studying brain tissue [1]. At present, MRE is the sole modality that can assess biomechanical properties of brain tissue non invasively and *in vivo* as both palpation and ultrasound elastography are prevented by the presence of the skull. MRE generates maps which represent the mechanical properties of soft tissue, called elastograms. Over the last decade, this technique has revealed important characteristics of tissue biomechanics in disease and health [1]. In patients and mouse models, MRE has demonstrated significant stiffness alteration in Alzheimer's disease [2], Parkinson's disease [3], multiple sclerosis [4], traumatic brain injury [5], maturation [6], demyelination [7], and brain tumors [1, 8, 9]. Despite its success, cerebral MRE in preclinical research is still under-developed in terms of scan time and image quality. Although MRE in clinical and preclinical settings is based on the same principles of magnetic resonance imaging (MRI) and motion encoding, clinical MRE outperforms murine MRE in detail resolution, scan time and data consistency [1, 10, 11].

Preclinical MRI scanners with high magnetic field are optimized for brain imaging. In general, brain images obtained with preclinical scanners have a higher quality than images obtained with human scanners at a low magnetic field. However, despite the significant advantages of the scanner, the overall quality of elastograms obtained in the mouse is lower than those of the human brain. The reasons for this are related to the sub-optimality of the applied preclinical MRE modalities, which are still based on slow multi-shot data acquisition and noise-sensitive single-frequency reconstruction [12, 13, 14, 15]. While in human MRE fast single-shot acquisition with noise robust post-processing has now been used for more than a decade, MRE in preclinical settings is based on slow multi-shot acquisition combined with noise-sensitive viscoelastic reconstruction methods [1]. The slow data acquisition prevents the application of noise-robust multifrequency reconstruction methods that generally need significantly larger data sets than classical single-frequency reconstruction.

The overall aim of this PhD project was the development of a methodology for fast, multifrequency brain elastography in the mouse, with high spatial resolution. To this end, a fast, new, single-shot MRE sequence based on spin-echo echo-planar imaging (EPI) [16] was

implemented and combined with multifrequency tomoelastography post-processing [17]. In this dissertation, I will introduce the newly-created modality. I will than summarize its performance in comparison to state-of-the-art mouse brain MRE and demonstrate its feasibility for *in vivo* studies. As will be shown, the new method retrieves the mechanical properties of the mouse brain in a shorter scan time and with greater detail resolution than conventional MRE. Thanks to the single-shot acquisition technique implemented, the method reduces scan time significantly and allows for the monitoring of dynamic stiffness changes, with high temporal resolution. Moreover, multifrequency sampling of wave fields improves the spatial resolution of the stiffness maps, according to the principle of multifrequency dual inversion techniques [1, 17]. The improvements will be demonstrated through studies of hypothermia and brain death in mice.

1.1. Hypothermia

Therapeutic hypothermia, in which body temperature is decreased to below its normal level, has been successfully used to minimize neuronal damage and improve outcomes in many injuries, including traumatic brain injury [5], spinal cord injury [18], stroke [19], and neonatal encephalopathy [20]. However, the biophysical mechanisms of hypothermia are largely unknown. Cerebral blood flow (CBF) [21] and water diffusion [22] are reduced in hypothermia. However, nothing is known about the effect of temperature on cerebral tissue stiffness and how changes in CBF, water diffusion, and brain stiffness correlate with one another [23]. Monitoring of dynamic stiffness changes with conventional preclinical MRE is made impossible by the long measurement time. Using our newly-developed imaging sequence [23], we monitored the temperature influence on brain stiffness with relative high temporal resolution [24]. Additionally, we correlated stiffness, diffusion, CBF and body temperature in the hypothermic to normothermic range for the first time [24].

1.2. Hypoxia

The lack of oxygen supply leads to irreversible loss of neurons and, after a while, to brain death. A few minutes after respiratory arrest (RA), the permanent death of brain cells leads to hypoxic-anoxic injury (HAI). Brain damage in patients after cardiac arrest (CA) accompanied with RA

has been extensively studied [25]. However, little is known about biophysical processes during HAI. Unlike during normal conditions or brain disease, brain pathology from RA progresses rapidly, within seconds or minutes. This highly dynamic process cannot be resolved by conventional brain MRE. Similarly, the temporal resolution of other imaging methods sensitive to structure and function such as diffusion weighted imaging (DWI), arterial spin labeling (ASL) or magnetic resonance (MR) spectroscopy (MRS) is in the range of 5 to 15 minutes [1, 16]. Using our novel method [23], we have monitored stiffness changes in the brain during death for the first time [26]. Additionally, we correlated *postmortem* mechanical changes with physiological imaging markers obtained by MRS, DWI, and T2*-mapping [26].

1.3. Outline

In the next chapter, I will briefly summarize MRE theory and the motivation of performing MRE in the mouse brain. In Chapter Three, the newly-developed MRE modality and the methods that were used for validation and *in vivo* studies are described. Chapter Four presents the results of three *in vivo* studies, while Chapter Five discusses them. Finally, Chapter Six summarizes the findings and Chapter Seven describes the author's contribution to the developed method and the studies conducted.

2. Theory

2.1. Magnetic resonance elastography

MRE is a phase-contrast MRI technique which uses the propagation of mechanical waves to determine tissue stiffness [1]. In MRE, waves in the tissue are generated by external mechanical vibration, the induced displacement is encoded using a conventional MRI scanner, and tissue mechanical properties are estimated from processing the measured displacement field.

2.1.1 Biophysical background

After deformation, a purely elastic medium immediately returns to its original state, while a purely viscous medium loses its shape once force is removed. Biological soft tissues are modelled as viscoelastic materials which exhibit both elastic and viscous characteristics. In biophysics, the shear modulus μ is a measure of stiffness that quantifies the tissue ability to resist shear deformation, while the bulk modulus K is a measure of tissue resistance to compression. Due to the relatively low compressibility of biological tissues, incompressibility is assumed, making μ the preferable parameter for tissue stiffness quantification [9].

Biological tissues exhibit viscous and elastic properties at the same time. Therefore, for viscoelastic materials, μ is a complex quantity denoted by G*=G'+G'', and called the complex shear modulus with G' and G'' being the real and imaginary parts, respectively. G' is called the storage modulus, and it is a measure of the elastic behavior of the tissue. G'' is called the loss modulus, which is related to tissue viscosity.

A purely elastic media can be modelled with a massless spring. The stress-strain relation of the spring model in one dimensional case is

$$\sigma_e = E\epsilon \qquad \text{(Eq. 1)}$$

with σ_e being the stress into the direction denoted by vector e, E the Young's modulus and ϵ the resulted strain [1]. Strain is the change in length relative to the original length L_0 of the spring:

$$\epsilon = \frac{\Delta L}{L_0}. \qquad \text{(Eq. 2)}$$

In contrast to an elastic medium, a purely viscous medium is modelled with a dashpot filled with viscous fluid and with a piston that can move through the fluid [1]. The stress-strain relation of the dashpot model is

$$\sigma_v = \eta\dot{\epsilon} \qquad \text{(Eq. 3)}$$

with σ_v being the stress in the volume denoted by v, η the viscosity of the fluid and $\dot{\epsilon}$ the rate of change of the strain.

In the Laplace domain, G* represents the stress-strain ratio by

$$\overline{G^*}(s) = \frac{\bar{\sigma}(s)}{\bar{\epsilon}(s)} \qquad \text{(Eq. 4)}$$

with $\overline{G^*}(s)$ being the complex shear modulus, $\bar{\sigma}(s)$ the stress and $\bar{\epsilon}(s)$ the strain in the Laplace domain [1]. $\overline{G^*}(s) = E$ for the spring and $\overline{G^*}(s) = \eta s$ for the dashpot. In the frequency domain, the Laplace domain variable s can be substituted by s = iω and the resulting quantity $\overline{G^*}(\omega)$ can be interpreted as the measure of viscoelastic properties of the tissue, if an oscillating strain is applied with angular frequency ω [1].

Spring and dashpot models can be combined to model materials with hybrid characteristics [1]. In parallel arrangement of one dashpot and one spring component with complex moduli G_1* and G_2*, respectively, the strain is always constant in the model while the total stress is the sum of the stresses in the two components, as given by equations 5 and 6. The parallel arrangement of one spring and one dashpot is called the Kelvin-Voigt model [1].

$$\bar{\epsilon}(s) = \bar{\epsilon_1}(s) = \bar{\epsilon_2}(s) \qquad \text{(Eq. 5)}$$

$$\bar{\sigma}(s) = \overline{\sigma_1}(s) + \overline{\sigma_2}(s) = \overline{G^*}(s) \cdot \bar{\epsilon}(s) = \left(\overline{G_1^*}(s) + \overline{G_1^*}(s)\right) \cdot \bar{\epsilon}(s)\,. \qquad \text{(Eq. 6)}$$

In serial arrangement of one dashpot and one spring component the stress is constant, while the total strain is the sum of the strains in the two components, as shown by equations 7 and 8. The serial arrangement of one spring and one dashpot is called the Maxwell model [1].

$$\bar{\sigma}(s) = \overline{\sigma_1}(s) = \overline{\sigma_2}(s) \qquad \text{(Eq. 7)}$$

$$\bar{\epsilon}(s) = \bar{\epsilon_1}(s) + \bar{\epsilon_2}(s) = \frac{\bar{\sigma}(s)}{\overline{G^*}(s)} = \frac{\bar{\sigma}(s)}{\frac{1}{\overline{G_1^*}(s)} + \frac{1}{\overline{G_2^*}(s)}}\,. \qquad \text{(Eq. 8)}$$

While the Kelvin-Voigt and Maxwell models are capable of representing viscoelastic properties, they are both too simple for modelling real viscoelastic materials. Therefore, in

classical viscoelastic models of soft biological tissues, the number of spring and dash-pot elements is increased to increase the degrees of freedom in the models. The spring-pot model is a viscoelastic model with an infinite number of spring and dash-pot elements [1]. The stress-strain relation in spring-pot is given by:

$$\bar{\sigma}(s) = E^{1-\alpha}(s \cdot \eta)^{\alpha} \cdot \bar{\epsilon}(s) \quad (0 \leq \alpha \leq 1). \qquad \text{(Eq. 9)}$$

2.1.2 Time-harmonic wave fields

In soft biological tissue, two types of acoustic waves are induced by mechanical vibration: longitudinal waves and shear waves. The shear modulus μ and Lamé's second parameter λ are measures of tissue deformation induced by shear and longitudinal strain. Modelling the medium as infinite, homogeneous, viscoelastic, and isotropic material, the equation of harmonic motion is given by

$$\rho \frac{\partial^2 \boldsymbol{u}}{\partial t^2} = \mu \nabla^2 \boldsymbol{u} + (\lambda + \mu) \nabla (\nabla \boldsymbol{u}) \qquad \text{(Eq. 10)}$$

with ρ being the density of the material, **u** the vector displacement of the material, μ the shear modulus and λ the second Lame's constant [27]. Using equation 10, the determination of displacement **u** is straightforward, provided that μ and λ are known. This procedure solves the forward problem while the corresponding inverse problem involves the estimation of μ and λ based on **u**. This inverse problem is ill-posed. Assuming incompressibility of the material $\nabla(\nabla \boldsymbol{u})$ becomes negligibly small and we can drop the second term on the right side of equation 10 which gives the Helmholtz equation [27]

$$\rho \frac{\partial^2 \boldsymbol{u}}{\partial t^2} = \mu \nabla^2 \boldsymbol{u} \qquad \text{(Eq. 11)}$$

As mentioned earlier, in viscoelastic biological tissue models, the shear modulus μ is a complex quantity denoted by G*. Therefore, equation 11 can be written as

$$\rho \frac{\partial^2 \boldsymbol{u}}{\partial t^2} = G^* \nabla^2 \boldsymbol{u} \, . \qquad \text{(Eq. 12)}$$

G* is related to the shear wave speed (SWS) in the tissue by

$$SWS(\omega) = \frac{1}{\mathrm{Re}\left(\sqrt{\frac{\rho}{G^*(\omega)}}\right)} = \sqrt{\frac{2\,(G'^2 + G''^2)}{\rho\,(G' + \sqrt{G'^2 + G''^2})}} \qquad \text{(Eq. 13)}$$

with ω being the angular drive frequency of the mechanical vibration, G' the real and G'' the imaginary part of the complex G* [1].

2.1.3 Measurement of harmonic displacement fields by MRE

Figure 1 briefly summarizes how an elastogram is generated with MRE. The measured phase images capture the wave propagation at different time points of the vibration period. In the following step, the fundamental harmonic component of the displacement is extracted through temporal Fourier transformation of the measured phase images. Finally, the inverse problem is solved for G*, based on the displacement field.

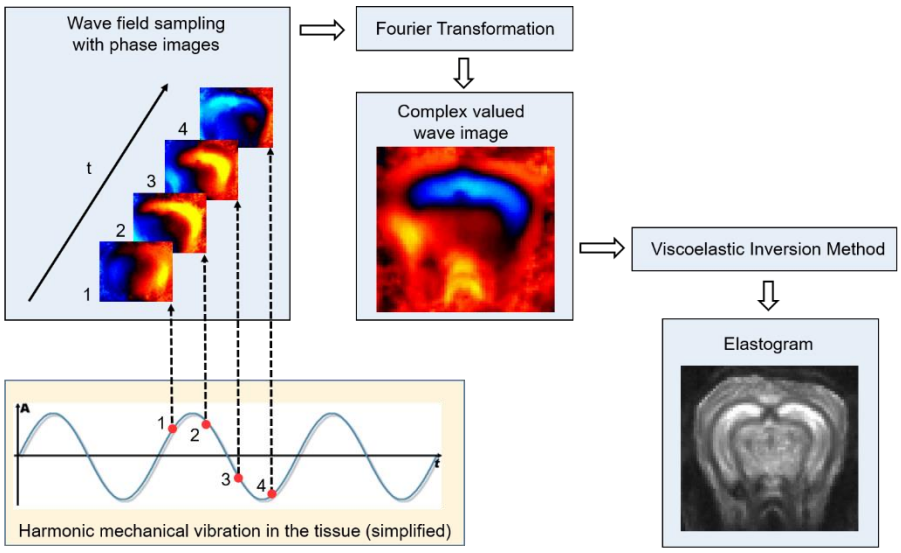

Figure 1. Elastogram reconstruction in the mouse brain. The harmonic displacement field in the tissue is sampled with phase images, which capture the wave propagation at different time points. The complex valued wave image (wave field) is obtained by Fourier Transformation of the measured phase images. In the last step, a viscoelastic inversion method generates the elastogram from the complex wave field.

In order to encode externally induced mechanical vibration into the phase image, the imaging sequence has to be equipped with motion encoding gradients (MEGs). In the presence of a gradient field $G_r(t)$, the motion of nuclear spins accumulates a phase shift ϕ, given by

$$\phi = \gamma \int_0^{\tau} G_r(t) \cdot r(t)\, dt \qquad \text{(Eq. 14)}$$

where γ is the gyromagnetic ratio, τ is the time duration of the gradient field, $G_r(t)$ is a temporal function of the magnetic gradient and r(t) is the position of the nuclear spins as a function of

time [28]. If the nuclear spins undergo harmonic motion during which $G_r(t)$ oscillates with the same frequency as the harmonic motion and τ is chosen such as

$$\int_0^{\tau} G_r(t)\, dt = 0 \qquad \text{(Eq. 15)}$$

then the motion of the spins is encoded into the phase of the magnetic resonance (MR) signal, with phase shift

$$\phi(\vec{r}, \theta) = \frac{\gamma n T(\vec{G} \cdot \vec{\xi_0})}{2} \cos\left(\vec{k} \cdot \vec{r} + \theta\right) \qquad \text{(Eq. 16)}$$

where r is the position vector, θ is the phase offset between applied motion and the MEG, n is the number of gradient cycles, T is the period of the MEG, G is the gradient amplitude, ξ_0 is the displacement amplitude and k is the wave vector [28].

The imaging sequence is a fundamental part of an MRE experiment, which i) controls the imaging parameters received from the user for consistency, ii) creates transverse magnetization using radio frequencies and gradients inside the MRI scanner, iii) encodes harmonic motion fields and iv) measures the MR signal. Imaging sequences in MRE are based on conventional MRI sequences. There are two main requirements for a MRE imaging sequence: it has to be synchronized with the external mechanical vibration and it has to be equipped with MEGs as described by equation 14. As illustrated in Figure 1, the wave field is sampled in consecutive scans by applying the MEGs at different time points over a vibration period. Typically, the wave field for a drive frequency is sampled with 4-8 phase images. The synchronization between the imaging sequence and the external vibration enables to apply the MEGs at an exact time point of a vibration period and is therefore inevitable for MRE. Synchronization is achieved by synchronizing the wave generator with the inner clock of the MRI scanner. A more comprehensive introduction to the imaging sequences used in MRE can be found in [1, 9, 10, 11, 28].

The wave propagation depends on individual tissue characteristics. For example, in a muscle, the external vibration causes a displacement that is different along the muscle fibers than perpendicular to them. Therefore, in three-dimensional (3D) full-field MRE, the displacement is measured in all three spatial dimensions and tissue mechanical properties are derived from the 3D wave field measured [1]. 3D wave fields can be measured either by switching the gradients in consecutive scans along the spatial dimensions or by using the recently published sample interval modulation (SLIM) encoding technique [29]. In SLIM, the MEGs are applied into all three spatial dimensions at the same time and the full 3D wave field is sampled at once.

This decreases the scan time by a factor of three when compared to consecutive 3D wave field sampling.

2.1.4 Stiffness reconstruction

The mechanical properties of the tissues are depicted by maps of G', G'' or SWS, also called elastograms. In some studies, the absolute value and the phase angle of the complex shear modulus are estimated, denoted by abs(G*) and φ, respectively. In statistical analysis, the term *stiffness* is used to describe absolute changes in abs(G*) or SWS.

In conventional inversion methods, the pressure waves are eliminated from the measured wave field and G* is computed from the remaining shear wave field. The effect of longitudinal waves can be removed by the Curl processing of the displacement field. Applying a curl operator to equation 10 yields

$$\rho \frac{\partial^2 \nabla \times \boldsymbol{u}}{\partial t^2} = G^* \nabla^2 (\nabla \times \boldsymbol{u}) \qquad \text{(Eq. 17)}$$

where $\nabla \times \boldsymbol{u}$ is the curled displacement field and ∇^2 the Laplace operator [1, 27].

We distinguish between two groups of reconstruction methods for estimating tissue mechanical properties: single-frequency inversion and multifrequency inversion. Local frequency estimation (LFE) and algebraic Helmholtz inversion (AHI) are the most widely-used single-frequency reconstruction methods [1, 9, 10]. While single-frequency inversion can be applied to data that was measured using a single vibration frequency, it has a limited spatial resolution and is unstable in the presence of noise and low SNR due to the calculation of higher order derivatives [1]. This issue can be ameliorated by the use of averaging over several distinct vibration frequencies, as used in multifrequency MRE [17]. Elasto-visco inversion (MDEV) and *k*-based multifrequency-dual elasto-visco inversion (*k*-MDEV) are the most widely-used multifrequency inversion methods [1].

Each inversion method has its advantages and disadvantages. For state-of-the-art mouse brain MRE AHI is used, which computes G* through direct inversion of the Helmholtz equation (Eq. 12) [1, 11]. AHI is affected by the well-known dispersion-by-inversion problem in MRE [1]. This problem addresses the systematic bias of G* or SWS values in homogeneous materials, as derived from finite-difference based inversion. AHI uses finite derivative operators of a second order, which gives rise to an apparent viscoelastic dispersion even in the ideally elastic case.

As analyzed in several MRE studies, an overestimation of values is encountered when the waves have a low support of less than eight pixels per wavelength, and values are lower than expected with high support and in the presence of noise [1]. In human MRE, phase gradient methods are used as alternatives to LFE and AHI for viscoelastic reconstruction. Multifrequency MRE with *k*-MDEV post processing is a relative new phase gradient method, also called tomoelastography in the literature [17]. Tomoelastography reconstructs frequency-averaged SWS maps based on estimations of the wave number of single-directional components (plane waves) in frequency averaged wave fields. A more comprehensive introduction to inversion methods in MRE can be found in [1, 9, 10].

2.1.5 Mechanical excitation

Mechanical waves are induced into the tissue by external drivers that can be electromechanical, piezoelectric, or pneumatic. The driver is often synchronized to the clock of the scanner, in order to avoid any latency of the wave relative to the scanner after minutes of continuous vibration. For choosing the appropriate driver component, the desired frequency range is of great importance. The induced shear wavelength depends on the frequency of the external vibration source and on the medium that the wave travels through. The adequate wavelength and, therefore, the optimal vibration frequency in MRE depends on the size and tissue structure of the organ, and has to be chosen carefully. In human brains with ca. 15 cm length, typical excitation frequencies range from 10 to 100 Hz, with amplitudes up to 1 mm. The most popular implementations are based on air cushions, loudspeakers or piezo actuators. The excitation frequency for the mouse brain with ca. 1.5 cm length needs to be much higher than in humans, generally in the range of 600 to 1800 Hz, with amplitudes on the micrometer scale. Only a few technical solutions exist which can create high-frequency vibrations and are at the same time suitable for preclinical MRI scanners. Here, the most common driver setups are based on Lorentz coils and piezoelectric elements. A more comprehensive introduction to the transducer systems used in MRE can be found in [1, 9, 10].

2.2. Motivation of MRE in the mouse brain

Numerous MRE studies in humans have reported mechanical differences between brain areas and alterations in viscoelastic parameters in various diseases [1, 9, 10, 11, 27]. This success

further motivated the application of MRE in rodents, in order to investigate viscoelastic tissue parameter changes in disease models and correlate them with histopathology [11]. The first mouse brain MRE was performed by Atay et al. in 2008 [12]. Since then, MRE in preclinical studies have given important insights into the connection between neuronal disease development and corresponding stiffness alterations [11]. It has been shown that neuronal cell density is one of the most important parameters affecting tissue stiffness, and therefore neuronal diseases causing neurodegeneration are characterized by significant tissue softening [2, 7, 8, 15]. Table 1 summarizes basic mouse brain MRE studies reported in the literature. A comprehensive review of mouse brain MRE, including findings, imaging sequences, actuator setups and inversion methods, can be found in [1, 11].

	Vibration frequency in Hz	SWS in m/s (mean ± standard deviation)	Resolution in mm (voxel size × voxel size × slice thickness)	Scan time for one wave field component
Atay et al. [12]	1200	3.93 ± 0.45	0.25×0.25×0.40	8
Clayton et al. [31]	600 - 1800	1.42 – 2.97	0.25×0.25×0.25	22
Jamin et al. [8]	1000	2.85 ± 0.04	0.15×0.15×0.30	8
Boulet et al. [14]	877.5	3.04 ± 0.04	0.16×0.16×1.00	60
Hain et al. [31]	900	2.35 ± 0.05	0.20×0.20×2.00	20
Klein et al. [15]	900	2.35 ± 0.12	0.20×0.20×2.00	20
Riek et al. [4]	900	2.56 ± 0.03	0.20×0.20×2.00	20
Millward et al. [32]	900	2.46 ± 0.13	0.20×0.20×2.00	12
Schregel et al. [7]	1000	2.86 ± 0.18	0.15×0.15×0.30	n.a.
Munder et al. [33]	900	2.65 ± 0.10	0.25×0.25×1.00	20

Table 1. Stiffness estimates of the mouse brain, measured by *in vivo* MRE and reported in the literature [23].

In general, high-field preclinical MRI scanners outperform clinical systems for brain imaging in terms of overall image quality, resolution and signal to noise ratio (SNR). Despite this, cerebral MRE in the mouse provided elastograms with less structural resolution than elastograms in humans. Reasons for this include the lack of time-efficient MRE sequences for preclinical MRI systems, as well as the use of single-frequency inversion methods. MRE of the mouse brain takes at least 20 minutes for one vibration frequency with full 3D wave field acquisition (see Table 1), resulting in a total scan time of about 100 minutes for five stimulation frequencies. By contrast, cerebral MRE in patients with five vibration frequencies, each with

eight dynamics and full 3D wave field acquisition, requires around 5 minutes [1]. Because of the unacceptably long scan time, in most of the published mouse brain MRE studies only one drive frequency has been measured, and thus noise-sensitive single-frequency reconstruction had to be used.

Instead of single-frequency inversion, noise-robust multifrequency phase gradient reconstruction methods can be used. However, in order to benefit from the performance of these methods, the full 3D wave field has to be measured at multiple vibration frequencies, which is not feasible due to the long scan time of the available imaging sequences. In clinical settings of cerebral MRE, EPI, one of the fastest sampling schemes available, has been used since more than a decade for fast data acquisition [1, 9, 10]. After a single excitation pulse, EPI can acquire either an entire image (single-shot EPI) or several image lines (segmented EPI), which drastically reduces overall scan time [16]. In MRE, this gain can be reinvested in the acquisition of more vibration frequencies. However, B_0 inhomogeneity caused by steep changes of susceptibility in the tissue do not favor EPI and can lead to image artefacts, especially in regions adjacent to air-filled cavities [16]. B_0 inhomogeneity is not an issue at 1.5-T, but it gains importance at 3-T and beyond [1, 16]. The relatively small mouse brain is enclosed by small air-filled cavities that, in high field EPI, can cause significant image distortions. On the other hand, modern preclinical MRI scanners have advanced methods for B_0 shimming, and can attenuate the distortion effect of EPI. Cerebral MRE with EPI has already been performed successfully on clinical MRI scanners at high magnetic field of 7-T [30], a further indication that MRE with EPI in the mouse brain should be feasible.

While limited in the human brain, in abdominal organs, multifrequency MRE with *k*-MDEV post processing has been demonstrated to be noise-robust and provides elastograms with higher resolution and consistency than LFE or AHI [17]. Figure 2 illustrates the performance of *k*-MDEV against AHI in the human abdomen, using images from [17]. Tomoelastography resolves the anatomical details with a resolution of the underling imaging matrix similar to the T2 weighted magnitude image and significantly outperforms AHI [17]. However, tomoelastography is limited by the complexity of the human brain resulting in artefacts on the elastograms [1, 23]. The human brain is characterized by a dense vascular system, sulci and folded cortex. The presence of solid-fluid interfaces in the tissue disturbs the directional filters of *k*-MDEV, due to sharp changes in local wave numbers [1]. On the other hand, the mouse brain is less folded and has fewer sulci than the human brain, which favors tomoelastography.

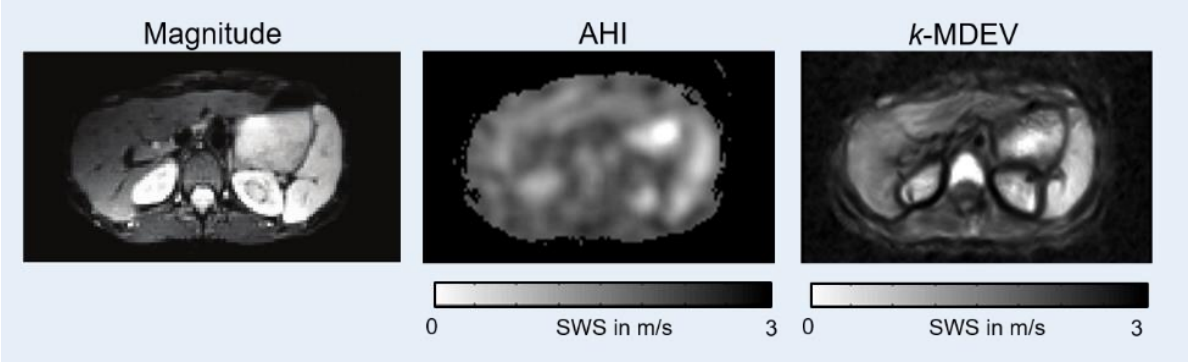

Figure 2. Multifrequency MRE with *k*-MDEV post-processing in the human abdomen [17]. Tomoelastography (k-MDEV) resolves the anatomical details similar to the magnitude image and significantly outperforms algebraic Helmholtz inversion (AHI).

2.3. Hypothesis of the PhD work

The overall hypothesis of this PhD work was that multifrequency MRE with tomoelastography post-processing provides high-resolution maps of stiffness of the mouse brain. The quality of these maps should improve compared to classical single-frequency MRE. In order to acquire multifrequency MRE data within a short time, as required by tomoelastography, a new single-shot MRE imaging sequence was developed based on EPI image acquisition [16] and SLIM motion encoding technique [29]. As a consequence, this should enable previously inaccessible, spatially and time-resolved studies to investigate important fundamental interactions between physiological effects and viscoelastic parameters.

3. Methods

3.1. Tomoelastography of the mouse brain

3.1.1 System configuration

The system configuration is illustrated in Figure 3. Tomoelastography of the mouse brain was developed for a 7-T small animal MRI scanner (Bruker BioSpec 70/16, Ettlingen, Germany) using a 20-mm diameter 1H-RF quadrature volume coil [23]. The scanner was synchronized to a low-current transistor-transistor logic function generator (CGC Instruments, Chemnitz, Germany) based on a 10-MHz harmonic signal. The function generator was connected to the trigger output of the scanner and was controlled by the imaging sequence with trigger signals. The trigger signals select and initiate the desired mechanical vibration with the desired frequency. This strategy, called smart triggering [1], makes it possible to define and run multifrequency measurements without any user interaction during the measurements.

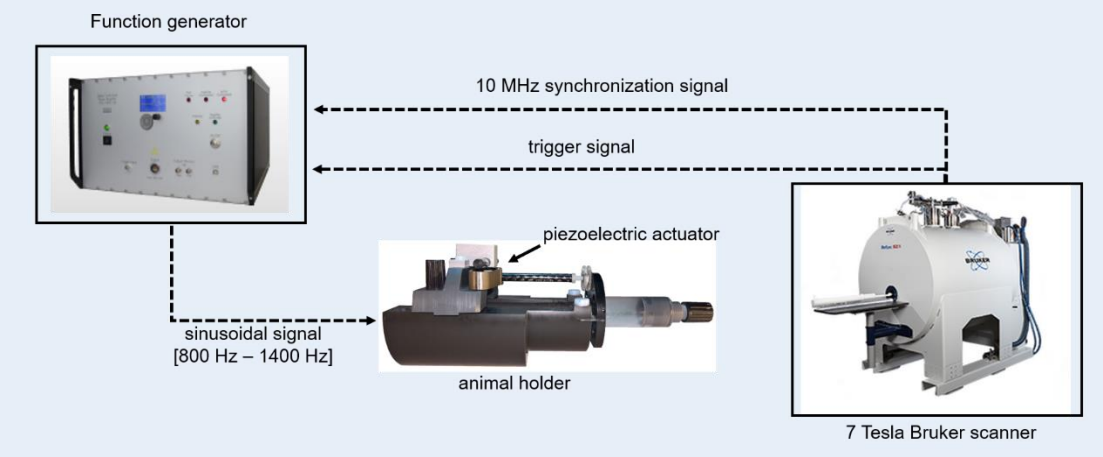

Figure 3. Setup for *in vivo* MRE of the mouse brain. The mechanical vibration was generated with a piezoelectric actuator. A low-current function generator was synchronized to a 7-T small animal MRI scanner and controlled with trigger signals from the imaging sequence. The function generator supplied sinusoidal low-current signal for the piezo element, which was embedded into the animal holder.

Figure 4a shows the major components of the custom-made animal holder. The mechanical vibration was created with the integrated piezoelectric actuator (APA200 NM, CEDRAT Technologies, Meylan Cedex, France), which was supplied with sinusoidal low-current signal from the function generator. The amplitude of the created displacement was approximately 60

µm peak-to-peak and its direction was perpendicular to the principal axis of the magnetic field of the scanner. The vibration was transferred into the head cradle of the animal holder through a carbon fiber rod. Figure 4b illustrates the setup with an animal. Figure 4c shows the position of the mouse head in the head cradle.

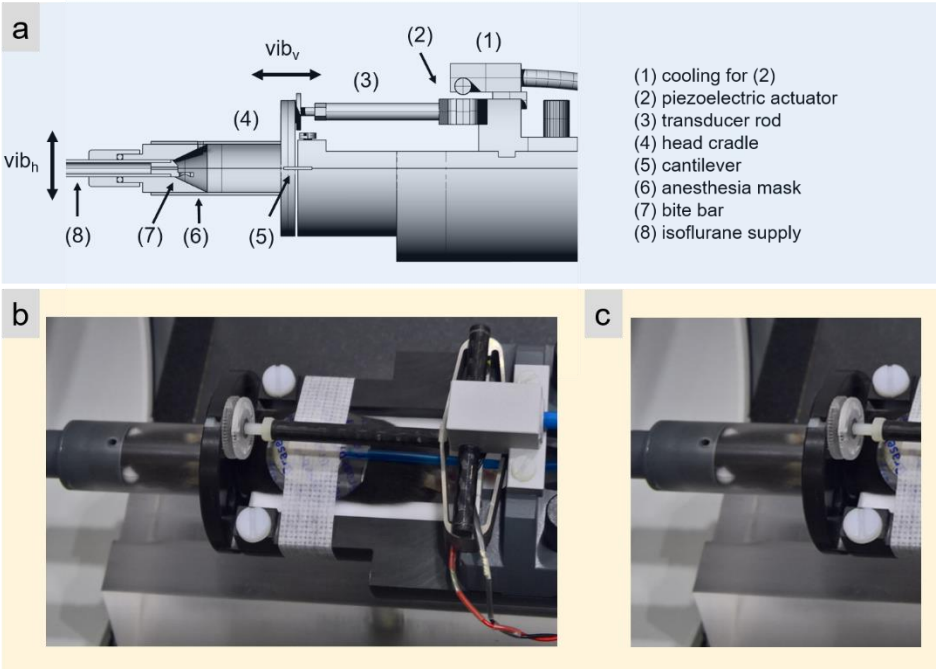

Figure 4. (a) Major components of the MRE transducer system including cooling for the piezoelectric actuator [23]. The vertical vibration created by the piezo element (vib_v) is turned into horizontal vibration (vib_h) by the cantilever connection between the body holder and the head cradle. (b, c) The position of the mouse head inside the anesthesia mask with the eyes covered with ointment against drying out [23].

3.1.2. Single-shot imaging sequence: EPI-MRE

ParaVision6.1, the vendor-provided software environment of the 7-T small animal scanner, offers the possibility to create new imaging sequences through its interface. I developed the novel single-shot EPI-MRE imaging sequence with asymmetrical motion encoding. Figure 5 shows the pulse sequence diagram for one repetition block. The principle of EPI-MRE was identical to conventional EPI [1, 16]. The transverse magnetization was created with a 90º excitation pulse and refocused after TE/2 with a 180º refocusing pulse in order to obtain a spin echo at TE. External mechanical motion was encoded into the phase of the MR signal with sinusoidal MEGs inserted between the excitation and refocusing pulses. Wave fields could be sampled either in one spatial direction or in all three directions simultaneously by SLIM motion

encoding [29]. EPI image acquisition with conventional Cartesian imaging centered on the time point of echo formation was used, as described in [16].

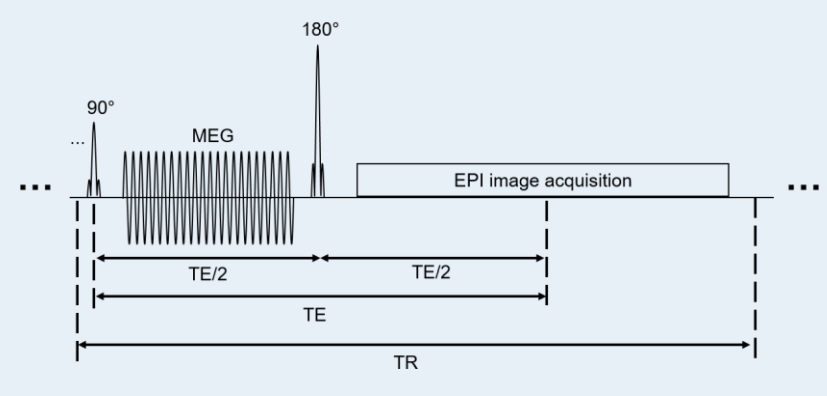

Figure 5. Single-shot spin-echo EPI-MRE pulse sequence [23]. The motion-encoding gradients (MEGs) are deployed prior to the 180° refocusing pulse. The number of MEG cycles can be adjusted by the user.

3.2. Validation and performance analysis

The stability of the MRE modality developed was validated with phantom experiments and simulations. Additionally, the performance of tomoelastography was compared to that of AHI.

Two cylindrical phantoms made of ultrasound gel (Sonogel, Germany) were investigated at room temperature. One sample with 13.3 mm diameter was measured in the 7-T small animal MRI scanner with EPI-MRE. A second sample with 7.5 mm diameter was investigated in a compact 0.5-T tabletop MRE scanner, which we used as a reference standard [34]. Five drive frequencies (800, 900, 1000, 1100 and 1200 Hz) were used. The imaging parameters for the two scanners, which included TE, TR and image resolution were similar. SWS was reconstructed with three methods:

i) Cylindrical waves in phantoms were fitted based on Bessel functions [34]. This method was applied to the 7-T and 0.5-T data sets. The values obtained from the 0.5-T scanner were considered ground truth. SWS valued obtained from Bessel fit were additionally fitted with the spring-pot model yielding the model parameters μ (shear modulus) and α (dimensionless power-law exponent). The spring-pot model was chosen because this model most accurately describes the mechanical properties of the phantom material [1].

ii) AHI as detailed in [35] was applied to the 7-T data set. The complex shear modulus G*, the output of AHI, was converted to SWS by equation 13.

iii) Tomoelastography with *k*-MDEV inversion as described in [17].

For simulations, cylindrical waves from 800 to 1200 Hz were computed using a Bessel function of the first kind [34]. For the simulated waves, ground truth SWS of 3.5 m/s was assumed, which is close to measured *in vivo* mouse brain values in [23, 24, 26]. Mean SWS was computed for the entire cylindrical area, while SNR varied between 1.1 and 46. Spatial support N (pixels-per-wavelength as denoted in equation 1 in [36]) was approximately 20. Since N and SNR have adverse effects on apparent SWS [1], the ratio N/SNR was used in the analysis.

3.3. *In vivo* MRE studies

After validation, the feasibility of the new method was demonstrated in three *in vivo* studies using the 7-T preclinical MRI scanner:

- Study1: *Fast tomoelastography of the mouse brain by multifrequency single-shot MR elastography* [23]. In this study, regional stiffness differences in the brain were investigated in ten healthy C57BL-6 mice. SWS values for whole brain (WB), cortex (CO), corpus callosum (CC), hippocampus (HP) and diencephalon (DI) were derived.
- Study2: *The influence of body temperature on tissue stiffness, blood perfusion, and water diffusion in the mouse brain* [24]. In this study, the influence of body temperature on brain stiffness, diffusion and perfusion was studied in six healthy C57BL-6 mice. The mouse was slowly heated up from hypothermia (28 ± 0.5 °C) to normothermia (38 ± 0.5 °C) in a 1.5 hour-long rewarming process. During rewarming, stiffness, diffusion and perfusion were continuously monitored in WB, CO, HP and DI. Apparent diffusion coefficient (ADC) and CBF was monitored with DWI and ASL, respectively.
- Study3: *Biomechanical properties of the hypoxic and dying brain quantified by magnetic resonance elastography* [26]. In this study, stiffness alteration in WB and HP during the critical phase of dying was continuously monitored with 40-second temporal resolution in fourteen healthy C57BL-6 mice. Additionally, *post mortem* (PM) mechanical changes were correlated with physiological imaging markers, obtained by MRS, DWI, and T2* mapping.

Animals were placed into the custom-made animal holder in a prone position and fixed onto a bite bar enclosed by the head holder. The bite bar was connected to an anesthesia gas line and the animals were anaesthetized during the experiments, with 1.5% isoflurane in a gas mixture of 70% O_2 and 30% N_2O. Body temperature, respiratory rate and ECG were monitored using an MR-compatible animal monitoring system. Body temperature was measured with a fiber-optical endorectal probe (Small Animal Instruments Inc., Stony Brook, NY, USA). In Study1 and Study3, body temperature was maintained constant at 36 ± 0.5 °C, whereas in Study2 it was modulated by regulating the temperature of the circulating water warming pad integrated into the animal holder. Table 3 summarizes the main imaging parameters for MRE. The imaging parameters of the other modalities (DWI, ASL, MRS, T2*) can be found in the papers published [23, 24, 26].

Parameter	Study1	Study2	Study3
wave phases	8	8	8
MEG & vibration frequency	900 - 1400 Hz	1200 - 1400 Hz	1200 Hz
MEG amplitude	80%	80%	80%
MEG periods	25	30	25
MEG direction	r, p, s, consecutively	3D	3D
SLIM	off	on	on
TR	1.5 s	3 s	1.8 s
TE	67 ms	40 ms	54 ms
image matrix size	90 × 80	80 × 80	80 × 80
field of view	16.2 × 14.4 mm^2	12.8 × 12.8 mm^2	12.8 × 12.8 mm^2
voxel size	0.18 × 0.18 mm	0.16 × 0.16 mm	0.16 × 0.16 mm
slice thickness	1 mm	1 mm	1 mm
averages	2	1	1
scan time per MRE	8 min	90 sec	40 sec

Table 2. MRE imaging parameters for *in vivo* studies.

In Study3, MRI acquisitions (MRE, T2*, DWI, T2w, MRS) were carried out once *in vivo* and once 1.5 hour PM, while continuous series of short MRE scans (40 seconds long) were performed throughout the 1.5 hour long PM period. After completion of the *in vivo* baseline measurements, CA was induced with a lethal dose of ketamine/xylazine (10% ketamine hydrochloride, 2% Rompun) injection subcutaneously, while the animals remained

anaesthetized. Time points of RA and CA were recorded based on the loss of the respiratory and ECG signals respectively. In three animals, MRE was combined with DWI in an interleaved manner, in order to investigate the relationship between tissue stiffness and diffusion. In these animals ($mouse_{10}$, $mouse_{11}$, $mouse_{12}$), several MRE and DWI scans were performed one after another, for 1.5 hours continuously. SWS and ADC values were analyzed for the hippocampus (HP). The effect of potential brain swelling associated with AHI was investigated in two animals. In these animals ($mouse_{13}$, $mouse_{14}$), a cranial window (CW) ca. 1 mm posterior to the bregma and 1 mm to the left of the midline was created by a neurosurgeon (CW size ca. 4×4 mm). 5 minutes after RA, the scanning was halted for 15 minutes and the mouse was taken out of the scanner to open the CW. Afterwards, the mouse was placed back into the scanner and MRE scanning was continued. ADC, T2* time, metabolites and water content were assessed for the HP. SWS time course during death was determined for the whole brain (WB) and HP.

3.3.1. Post-processing and statistical analysis

Elastogram reconstruction and the post-processing of measured data was done entirely in Matlab (MathWorks, Natick, MA, USA). SWS maps were computed from the complex valued wave images, using *k*-MDEV inversion as described in [17]. Prior to reconstruction, a Gaussian filter of strength $0.17 * 10^{-3}$ was used to suppress noise in the phase of the MR signal. Wave numbers were reconstructed from plane waves obtained by applying 8 directional filters for each single-frequency, single-component wave image.

Regional SWS values were derived from different regions of interest (ROIs), which were drawn manually in Matlab by considering the magnitude image and the corresponding elastogram. Significance was tested either with Wilcoxon rank or with a signed rank test, using the built-in Matlab functions *ranksum* and *signrank*. For correlation analysis, Pearson's linear correlation coefficient (r) and its corresponding statistical significance value (p) were computed. For significance test and correlation analysis, p value below 0.05 was considered significant (* and ** correspond to $p < 0.05$ and $p < 0.005$, respectively).

In Study2, the statistical significance of SWS, ADC, and CBF changes between low and normal body temperature was analyzed. Two temperature intervals were defined: T_{hypo} from 28°C to 30°C and T_{norm} from 36°C to 38.5°C body temperature.

4. Results

4.1. Validation and performance analysis

4.1.1. Phantom experiments

The frequency resolved wave images acquired by the new EPI-MRE sequence at 7-T and by 0.5-T tabletop MRE for reference are shown in Figure 6. Figure 7a shows spring-pot fitting curves and spatially averaged SWS values for the wave images measured in Figure 6, obtained using Bessel fit, AHI and *k*-MDEV. SWS values obtained from Bessel fit and the spring-pot model curves agree well for the two MRI scanners (7-T: $\alpha = 0.17$ and $\mu = 600$ Pa vs. 0.5-T: $\alpha = 0.18$ and $\mu = 590$ Pa) [23]. Taking Bessel fit values as a reference, *k*-MDEV shows a slight overestimation of 4.1%, while the overestimation of AHI is 12.9% [23].

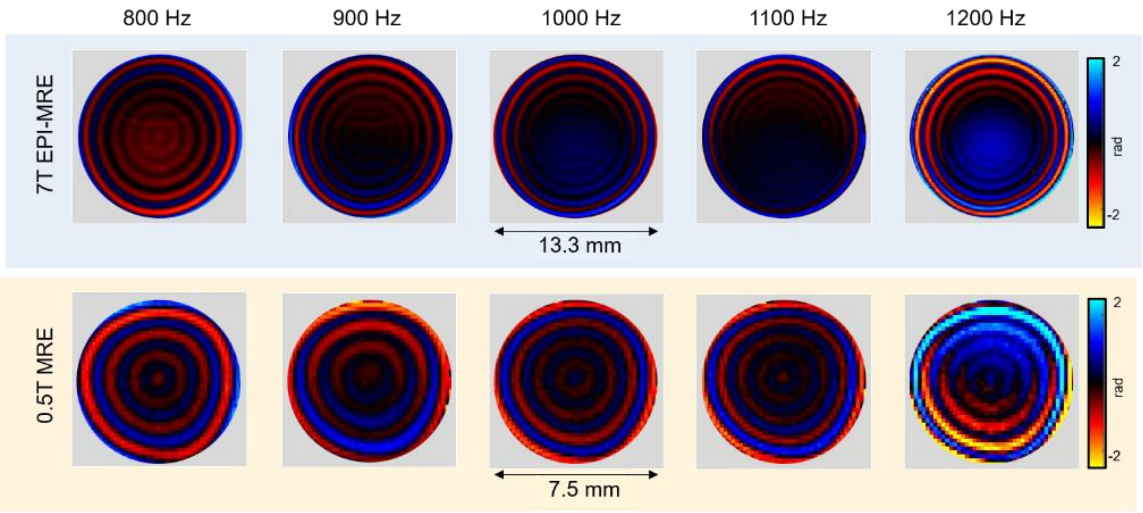

Figure 6. The real parts of the complex-valued wave images acquired with the 7-T and 0.5-T scanners in a frequency range from 800 to 1200 Hz [23].

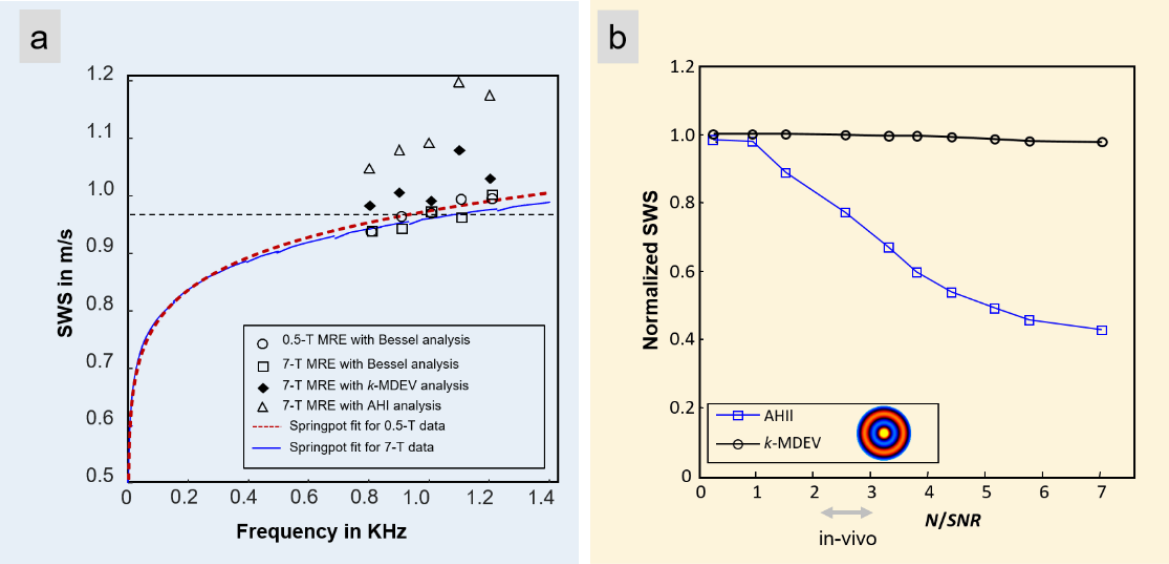

Figure 7. (a) Frequency-resolved shear wave speed in the gel phantom calculated by cylindrical wave fitting (Bessel fit), tomoelastography (k-MDEV), and algebraic Helmholtz inversion (AHI) of wave images shown in figure 6 [23]. (b) SNR analysis of AHI and *k*-MDEV based on wave simulations [23]. The ground truth is 1 due to normalization of SWS/SWS_0 with SWS_0 = 3.5 m/s as found by *in vivo* MRE. Gray arrows demarcate N/SNR ranges of experiments in the *in vivo* mouse brain.

4.1.2. Tomoelastography (*k*-MDEV) vs. AHI

The noise sensitivity of *k*-MDEV and AHI was analyzed in Figure 7b, with simulated waves and added noise. Dependent on the ratio *N*/SNR, the dispersion-by-inversion bias can cause either an over or an undershoot of values, both enhanced by second-order finite derivative methods such as AHI [1]. *k*-MDEV, being based on single order gradients, is less susceptible to the dispersion-by-inversion bias [1, 17]. While AHI is 15-30% below ground truth when applied to similar wavelengths as measured *in vivo* (*N*/SNR between 2 to 3), *k*-MDEV only has a 2% offset [23].

Figure 8 visually compares multifrequency tomoelastography with state-of-the-art MRE from [15]. Figure 8a shows the magnitude image and the corresponding AHI elastogram of G* measured with a modified fast low angle shot (FLASH) sequence at a single drive frequency of 900 Hz, with a 0.2 * 0.2 mm voxel size. The total scan time was approximately 20 minutes. By contrast, Figure 8b shows the magnitude image and the corresponding frequency averaged SWS map (six drive frequencies, from 900 to 1400 Hz with 100 Hz increment) measured with EPI-MRE with 0.18 mm * 0.18 mm voxel size [23]. The scan time for one frequency was approximately 80 seconds, giving a total scan time of approximately 8 minutes for all frequencies. Despite the significantly decreased scan time, multifrequency tomoelastography

resolves the anatomical details of the mouse brain with higher detail resolution than conventional AHI based MRE.

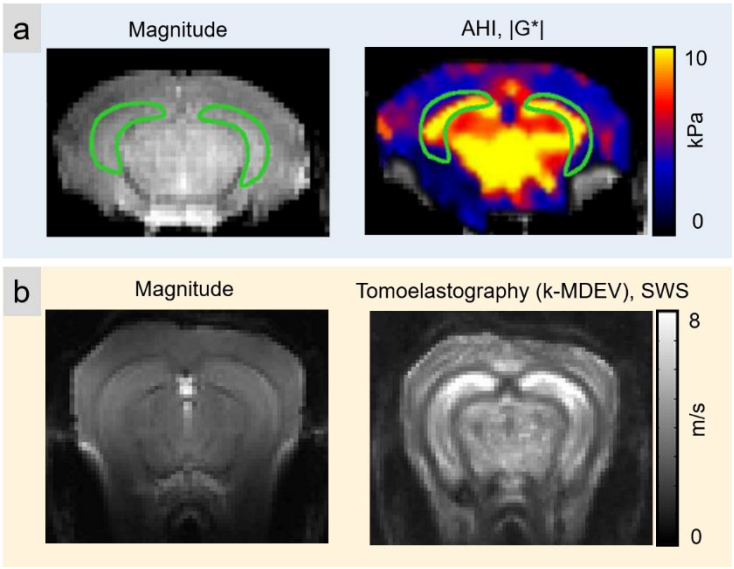

Figure 8. (a) Magnitude image and corresponding elastogram obtained by single-frequency (900 Hz) MRE based on a modified fast low angle shot (FLASH) sequence and algebraic Helmholtz inversion (AHI) [15]. The green ROI marks the hippocampus. (b) Magnitude image and corresponding elastogram obtained by multifrequency EPI-MRE (6 frequencies from the range of 900 – 1400 Hz, 100 Hz increments) with tomoelastography post processing [23].

4.2. *In vivo* MRE studies

4.2.1. Study1

Representative frequency-resolved complex-valued wave images (real parts) obtained in the same mouse are shown in Figure 9. The corresponding magnitude image and frequency averaged elastogram are shown in Figure 8b. Figure 10 shows the magnitude image of the measured slice position with the sub-regions, which were analyzed and the corresponding group mean SWS values calculated with *k*-MDEV and AHI [23]. Using *k*-MDEV, we measured SWS of 3.8 ± 0.3 m/s for WB with the highest values for HI (4.9 ± 0.5 m/s), followed in decreasing order by DI (4.8 ± 0.8 m/s), CO (3.5 ± 0.3 m/s), and CC (2.9 ± 0.2 m/s) [23]. AHI yielded SWS values of 2.7 ± 0.2 m/s for the WB with the highest values in CO (3.2 ± 0.2 m/s), followed in decreasing order by HI (2.9 ± 0.1 m/s), DI (2.7 ± 0.2 m/s), and CC (2.3 ± 0.1 m/s) [23]. AHI values for WB, CO, CC, HI and DI are approximately 30%, 6%, 21%, 41% and 44% lower

than *k*-MDEV values, respectively. The numerical analyses shown in Figure 7b allow us to relate this difference to an undershoot of true values by AHI [23].

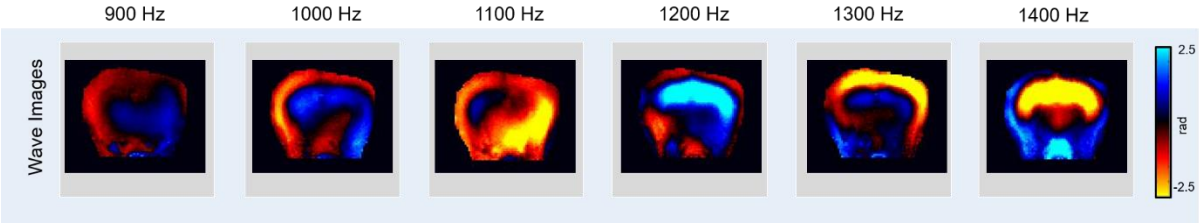

Figure 9. Frequency-resolved wave images measured in the same mouse (real part) [23]. The corresponding frequency averaged SWS map is shown in Figure 8b.

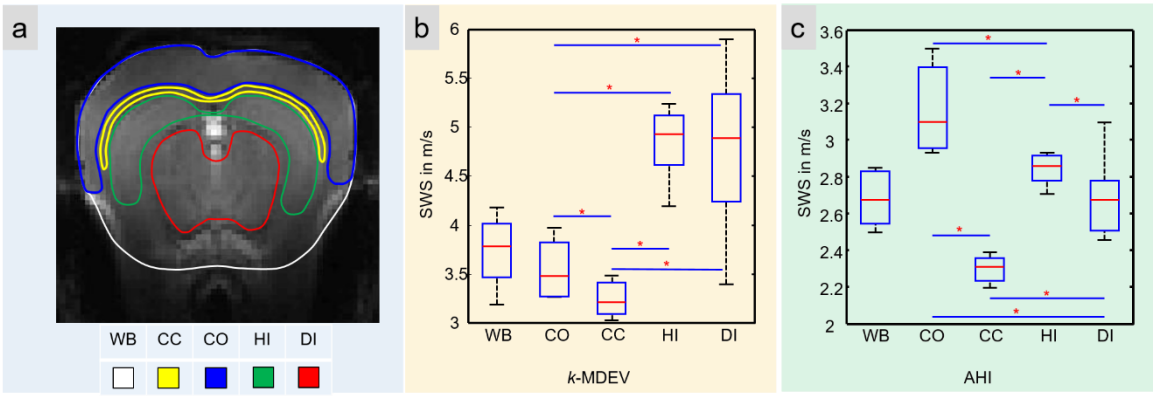

Figure 10. (a) Analyzed regions of interest (ROIs). (b), (c) Group values of SWS of *in vivo* mouse brain based on algebraic Helmholtz inversion (AHI) and tomoelastography (*k*-MDEV) for whole brain (WB), cerebral cortex (CO), corpus callosum (CC), hippocampus (HI), and diencephalon (DI) [23]. * indicates $p < 0.05$.

4.2.2. Study2

Figure 11 shows the magnitude image of the measured slice position and representative maps of SWS, ADC, and CBF. The relative decrease in SWS and the relative increases in ADC and CBF with temperature are already visually apparent [24].

Figure 12 shows temperature-resolved group mean SWS, ADC, and CBF values in the sub-regions analyzed. Except in DI, SWS was inversely correlated with temperature in all regions (WB: r = -0.94, CO: r = -0.85, HP: r = -92, all with **) [24], as shown in Figure 12a. Figures 12b,c show that ADC correlated with temperature in all regions (WB: r = 0.86, CO: r = 0.87, HP: r = 0.89, DI: r = 0.86, all with **), as did CBF (WB: r = 0.97, CO: r = 0.93, HP: r = 0.94, DI: r = 0.94, all with **) [24].

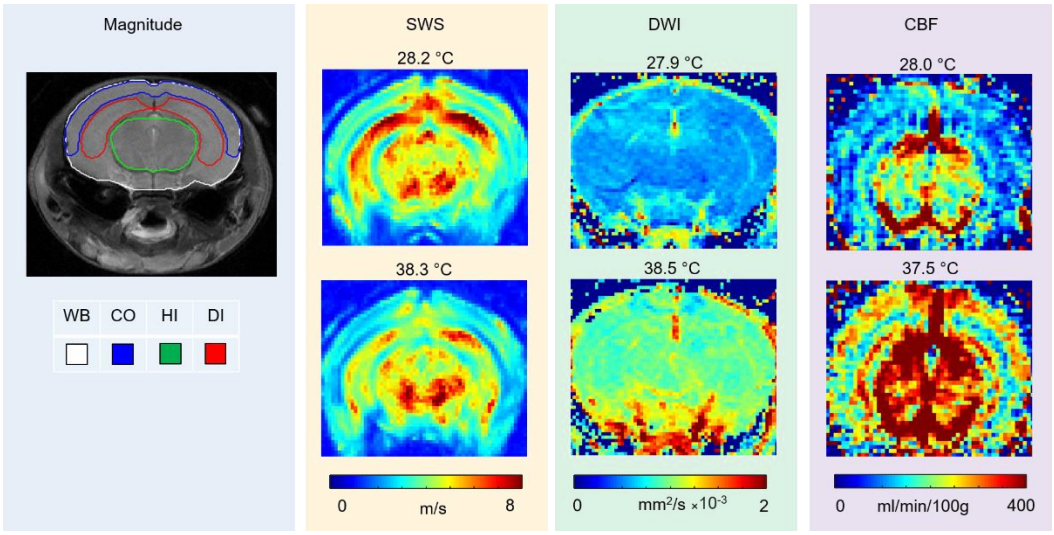

Figure 11. Representative *in vivo* maps of SWS, ADC, and CBF acquired at two temperatures - hypothermia and normothermia - in the same mouse [24].

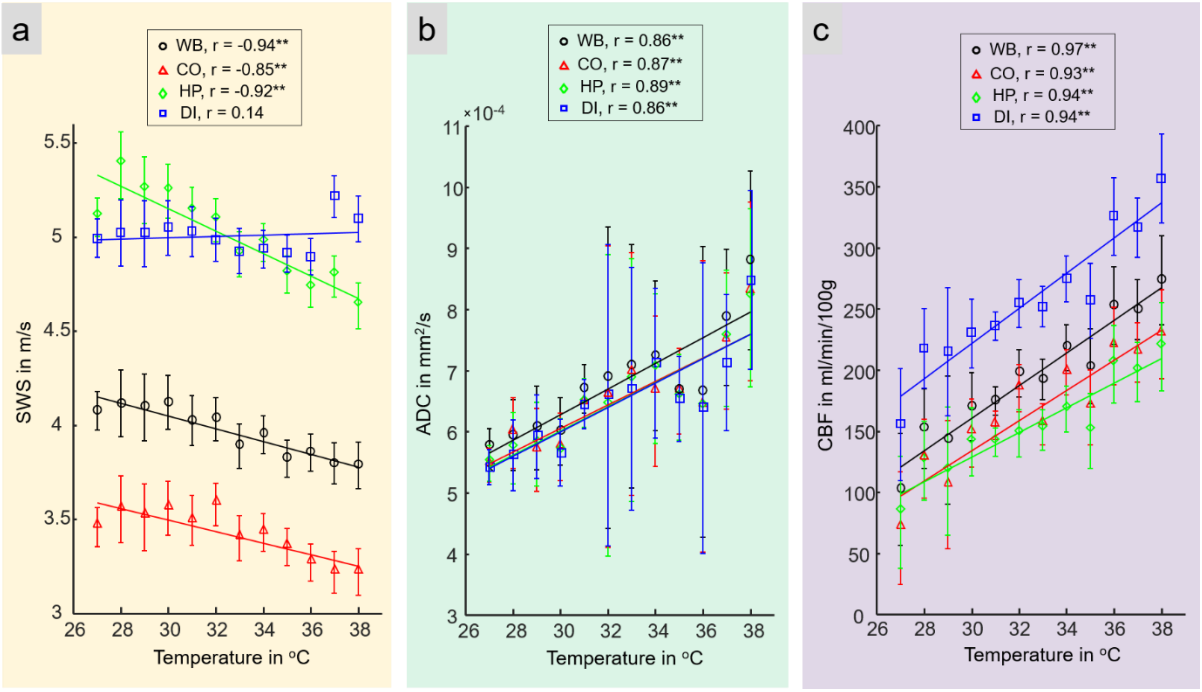

Figure 12. Temperature dependence of SWS (a), ADC (b), and CBF (c) in the analyzed brain regions for all mice examined (Pearson correlation coefficient, r) [24]. * and ** indicate $p < 0.05$ and $p < 0.005$, respectively.

Figure 13 presents relationships between ADC and SWS and between CBF and SWS for all the mice. The increase in ADC was linearly correlated with the decrease in SWS in WB (r = 0.8**), CO (r = -0.74*) and HP (r = -0.79**) [24]. No linear correlation was observed for ADC and SWS in DI. The increase in CBF was significantly correlated with a decrease in SWS in WB (r

= -0.84**), CO (*r* = -0.65*) and HP (*r* = -0.79**). No correlation was found between CBF and SWS in DI [24].

Figure 14 shows the effects of two body temperatures, T_{hypo} (28 °C ≤ T_{hypo} ≤ 30 °C) and T_{norm} (36 °C ≤ T_{norm} ≤ 38.5 °C), for SWS, ADC and CBF in all the mice [24]. From T_{hypo} to T_{norm}, mean SWS decreased by 6.2% in WB, 10.1% in CO and 7.4% in HP (all with *) [24]. No significant SWS change was observed for DI, while ADC and CBF increased in all the regions analyzed [24]. Mean ADC increased by 34% in WB, 31% in CO, 33% in HP, and 35% in DI (all with *) [24]. Mean CBF increased by 80% in WB, 82% in CO, 92% in HP and 60% in DI (all with *) [24].

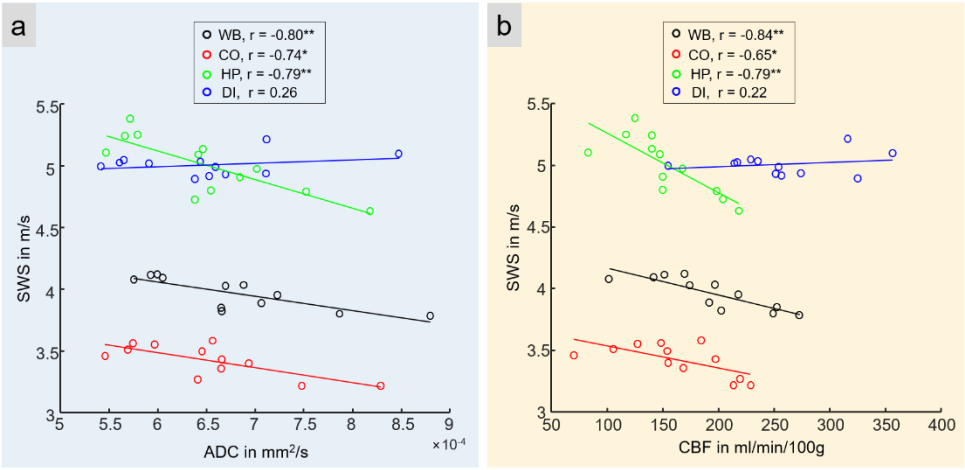

Figure 13. Correlation analysis (Pearson's r) between ADC and SWS (a) and CBF and SWS (b) for the analyzed brain regions [24]. * and ** indicate $p < 0.05$ and $p < 0.005$, respectively.

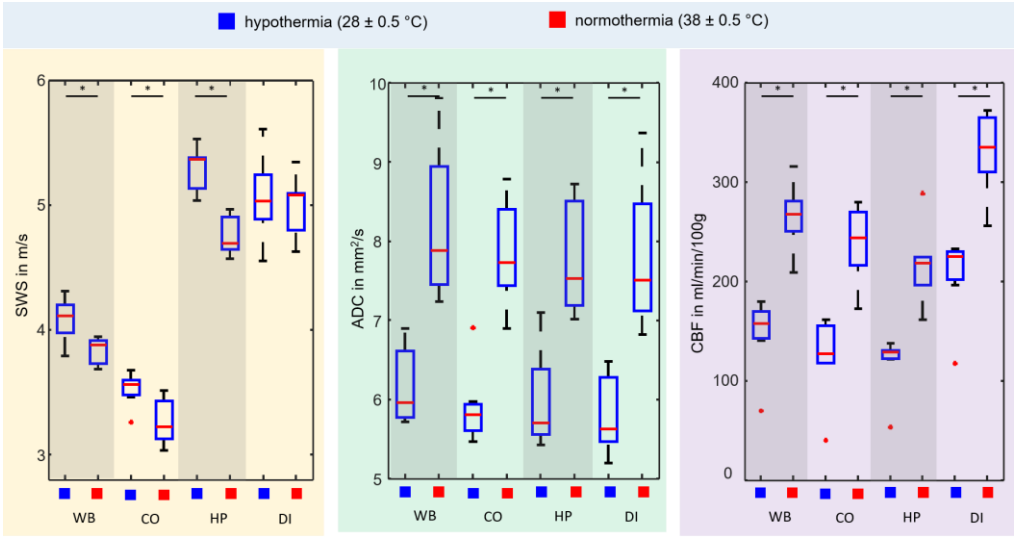

Figure 14. Changes in SWS (a), ADC (b), and CBF (c) during hypothermia in all mice [24]. * indicates $p < 0.05$ for the two-sided Wilcoxon signed rank test.

4.2.3. Study3

The average time between ketamine/xylazine administration and RA was 13 ± 4 min [26]. Figure 15 shows representative images of T2w, SWS, ADC, T2* and MRS *in vivo* and 1.5 h PM.

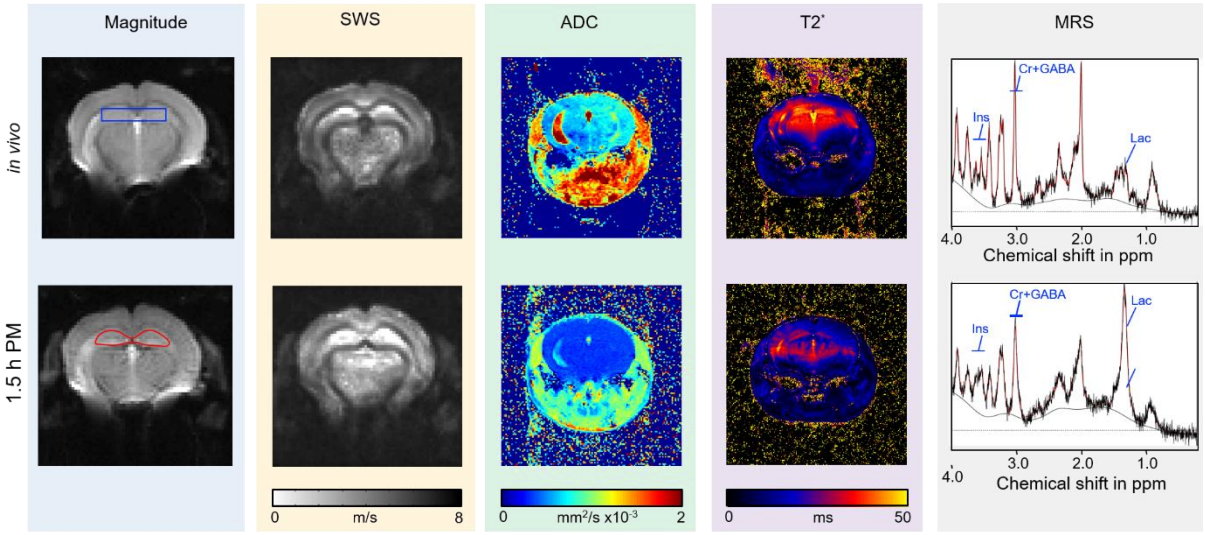

Figure 15. Representative *in vivo* and *post mortem* (PM) measurements of SWS, ADC, T2* and MRS spectra of the hippocampus acquired in the same mouse [26]. Hippocampus ROIs for MRS and other imaging methods (MRE, DWI, T2* mapping) are outlined in blue and red.

Figure 16a shows the time course of SWS between ketamine/xylazine injection and 1.5 h PM. Stiffness of WB and HP started to increase immediately after RA, while cardiac function was intact and reached a plateau approximately 5 minutes after CA [26]. After reaching its plateau, SWS remained relatively constant for the rest of the 1.5 hour measurement time. Group mean SWS increase was 6% in WB and 9% in HP (both with **) compared with *in vivo* values [26]. In Figure 16b, the ADC and SWS time course in the HP is shown in one animal. In the HP, the increase of SWS was correlated with a significant decrease of ADC in the three animals measured (Pearson *r* with -0.91, -0.95 and -0.97 for $mouse_{10}$, $mouse_{11}$ and $mouse_{12}$, respectively; all with **) [26]. Figure 16c reveals a decrease in stiffness after skull opening. SWS reduction in WB and HP compared to plateau values was 8.5% and 23.5% in $mouse_{13}$ and 10.0% and 26.7% in $mouse_{14}$, respectively [26].

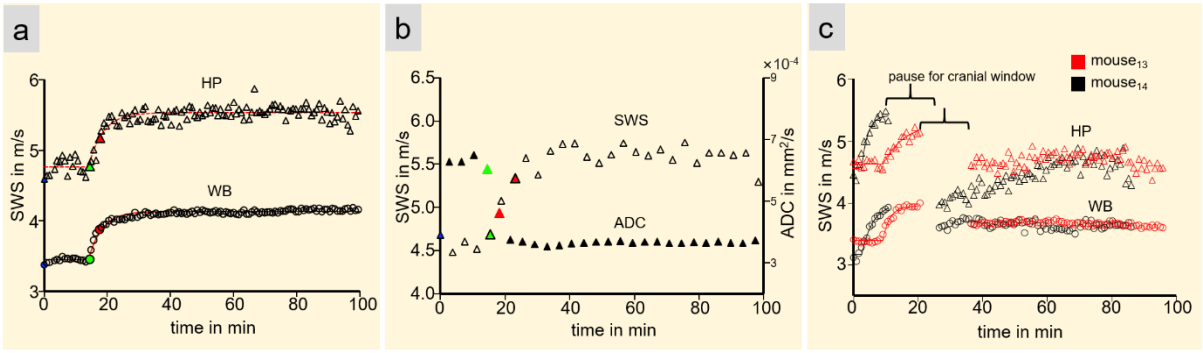

Figure 16. (a) Dynamic change in SWS in the whole brain (WB) and hippocampus (HP) due to hypoxic-anoxic injury (HAI) in one animal measured from the time point of ketamine/xylazine injection to 1.5 *post mortem* (PM) [26]. (b) Dynamic change in SWS and ADC in the whole brain after HAI [26]. (c) Effect of cranial window opening on SWS after HAI for two animals. Data points corresponding to respiratory and cardiac arrest are marked in green and red in (a, b) [26].

ADC decreased in all animals between *in vivo* and 1.5 hour PM, as shown in Figure 17a. We measured a significant group mean ADC decrease of 49% ± 6% (with **) between *in vivo* and 1.5 h PM [26]. Group mean value of T2* times was significantly higher *in vivo* than in 1.5 hour PM (with **), as shown in Figure 17b [26]. Water content measured with MRS increased in all mice between *in vivo* and 1.5 hour PM, as shown in Figure 17c [26]. Group mean water content was significantly higher 1.5 hour PM than *in vivo*. We measured a significantly elevated concentration of lactate (with **) [26].

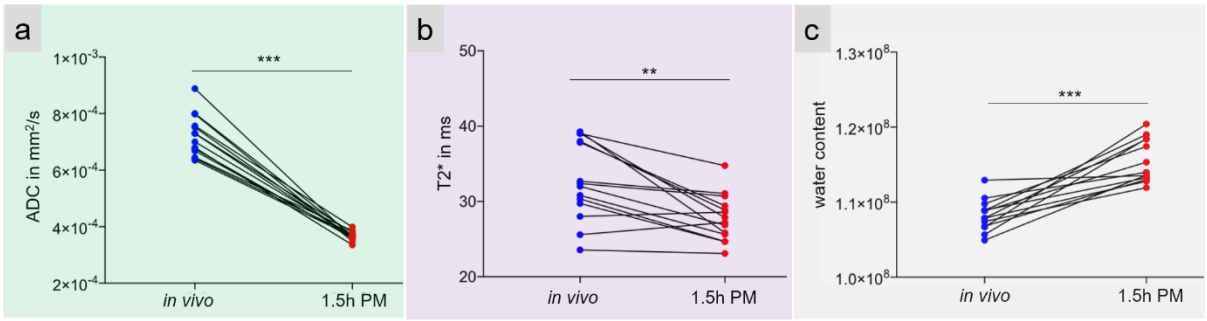

Figure 17. *Post mortem* changes in ADC (a), T2* (b), and water content (c) in all mice [26].

5. Discussion

Fast EPI-MRE combined with tomoelastography post-processing in the mouse brain was introduced. The method was validated with phantom experiments and simulations. The ground truth in phantom experiments was determined by Bessel fits of cylindrically emanating waves. This analytical solution of the wave equation in cylindrical coordinates avoids the discretization bias and is not susceptible to the noise-related underestimation of SWS values [1, 34]. We therefore used 0.5-T MRE as reference, as this modality is optimized for the generation and analysis of cylindrical waves [34]. This principle, implemented in our 7-T MRI scanner, gave similar results, suggesting the stability of the method for measuring ground truth values and the accuracy of the EPI-MRE sequence [23].

In addition to the validation experiments, the data set of *in vivo* measurements was reconstructed with AHI and resulting SWS values were compared with previously-reported values from the literature [23]. Table 1 gives an overview of SWS values obtained in the mouse brain using classical direct-inversion-based MRE. Our *in vivo* SWS value for the whole brain reconstructed with AHI agrees strongly with the values found in the literature, also indicating the accuracy of the established EPI-MRE sequence [23].

As shown through simulation experiments, AHI is more strongly biased by noise and discretization artefacts than single-derivative-based *k*-MDEV. In homogenous materials, such as the ultrasound gel used in phantom experiments, *k*-MDEV resolves ground truth values with significantly greater accuracy than AHI. These simulations and phantom experiments allow us to deduce that sub-regional differences between *in vivo* values of AHI and *k*-MDEV are due to significant underestimation of real values by AHI [23]. Additionally, by visually comparing the obtained mouse brain elastograms of *k*-MDEV to the ones found in the literature, multifrequency tomoelastography in the mouse brain increased the overall image quality and spatial resolution of elastograms similarly, as it increased in MRE of the human abdomen (see figures 2 and 8). Therefore, tomoelastography of the mouse brain supports a more detailed sub-regional analysis of *in vivo* stiffness maps than previous direct-inversion-based MRE.

In Study1, the relative stiffness difference clearly indicated the white matter (WM) of corpus callosum to be softer than cortical or hippocampal tissue [23]. This observation contradicts the published results of invasive ultrasound-based elastography in murine brains [37]. Corpus callosum is mainly composed of WM fibers, while the hippocampus has a large amount of grey

matter (GM). Our findings thus indicate that, in the measured central slice of the mouse brain, GM is stiffer than WM, unlike results for MRE in humans [30]. On the other hand, invasive atomic force microscopy, which is gold standard in biomechanics, also showed GM to be stiffer than WM in cerebral tissue, suggesting that brain stiffness is related to neuronal cell body density [38]. It was shown in [39] that deep GM in humans such as the putamen can be stiffer than WM, and that its stiffness is correlated with perfusion pressure. In the murine brain, our results show for the first time that a region which mainly contains GM is stiffer than the surrounding tissue which mainly contains WM [23].

The temperature-dependent changes in mechanical tissue properties observed in Study2 in several brain regions were found to correlate with CBF and ADC [24]. CBF and ADC courses measured during rewarming agreed strongly with the literature [24]. The overall increased blood volume at normothermia, as demonstrated by the ADC and CBF values, lead to tissue softening. In [39], tissue softening due to increased perfusion was reported for the deep GM regions including the thalamus and hippocampus. These findings suggest that increased blood perfusion, when accompanied by higher perfusion pressure, leads to an increase in overall tissue stiffness [24]. Our observation, that brain tissue stiffens in hypothermia when metabolic activity is reduced, might be communicated by the link between CBF and tissue viscoelastic properties. We hypothesized that the increase of fluid content of the tissue without nonlinear elastic expansion of vessel walls leads to tissue softening through increased fluidity [24]. We assumed that more blood per voxel is immersed in the brain at higher temperatures, while perfusion pressure does not change significantly [24]. Interestingly, stiffness of the diencephalon was not sensitive to temperature. This might indicate that blood vessels in diencephalon are less responsive and expand less with increasing temperature than vessels in other brain areas, resulting in increased perfusion pressure, which in turn could compensate for the fluidity-driven softening of brain tissue [24].

In Study3, using our novel fast single-shot EPI-MRE, we were able to monitor the progression of global and local cerebral mechanical variations from very early time points of respiration arrest up to 1.5 hours *post mortem* [26]. We observed a significant increase in stiffness within 40 seconds of respiratory arrest, while cardiac function was still preserved. Stiffness continued to increase during the first 5 minutes after respiration stopped, and remained relatively unchanged for the rest of the measurement time. Our results suggest that the stiffening of the brain during death can be mainly related to cytotoxic edema and brain swelling, both induced by hypoxia and post-respiratory-arrest anoxia [26]. Formation of cytotoxic edema is

characterized by the shifting of water from the extracellular into the intracellular space, leading to cellular expansion and consequently to water diffusivity reduction in the extra and intracellular spaces [40]. The restricted water movement is well reflected in the measured ADC course after respiratory arrest supporting the formation of cytotoxic edema, which is further supported by MRS [26]. The increased lactate level *post mortem* indicates Lactacidosis, which is a major mechanism underlying the development of cytotoxic edema [41]. In addition, the significantly increased water content 1.5 hours *post mortem* compared to *in vivo* values suggests that the water in the extracellular space was partially replenished by new water coming from insufficient cerebral blood circulation after respiration stopped. This extracellular edema, known as "ionic edema", results in brain swelling [40]. Brain swelling within the closed cranial cavity can increase the intracellular and intracranial pressure, which may contribute to the overall elevated cerebral stiffness [26]. This interpretation is further supported by experiments with cranial window opening, in which a partial decrease in stiffness was shown after a small cranial window was opened [26].

6. Summary

In summary, *in vivo* MRE of the mouse brain with multifrequency tomoelastography based on single-shot data acquisition by EPI-MRE was developed on a preclinical MR scanner. It was shown that tomoelastography generates elastograms of the murine brain with higher accuracy and more detailed resolution than classical MRE. Using the new technique, stiffness changes during the modulation of body temperature and during different phases of death were monitored for the first time. Furthermore, it could be shown that brain stiffness varies across different sub-regions of the brain with hippocampus stiffness being higher than stiffness values measured in the cortex and corpus callosum. In hypothermia, the *in vivo* measurement of cerebral blood flow and water diffusion indicated reduced brain perfusion and water mobility, which were inversely correlated to brain stiffness in hippocampal and cortical regions, while not correlated in inner brain regions such as the diencephalon. It could be demonstrated that EPI-MRE can measure subtle changes in stiffness during hypoxic-anoxic injury induced by respiratory arrest. It was demonstrated that brain stiffness had already increased 40 seconds after respiration arrest, and continued to increase during the critical phase of dying. DWI and MRS revealed that the mechanical signature of the dying brain is probably related to cerebral edema formation.

The new method contributes to the growing understanding of the mechanical behavior of brain tissues and has great potential for future studies of *in vivo* brain mechanical properties in health and disease. The method is currently being used in several ongoing studies. In a mouse model of multiple sclerosis, tomoelastography is being used to study brain stiffness alteration caused by inflammation and to identify regions with low-grade inflammation at their early stages. A further study investigates the effect of sport on neurogenesis and cerebral stiffness. In the future, EPI-MRE's application for monitoring the tumor growth in U87 and GL261 mouse models of glioblastoma is being planned.

7. Author's contribution

The core of this PhD project was the development of the single-shot EPI-MRE sequence for preclinical mouse brain MRE. EPI-MRE was entirely developed by me including sequence design, implementation and testing. I configured all hardware components (see Figure 4), optimized and synchronized the vibration hardware and the MRI scanner. I programmed the imaging sequence in C++ programming language and equipped it with MEGs (see Figure 5). I tested the sequence timing and I synchronized the sequence with the used function generator in order to avoid any latency between the MEGs and the external mechanical vibration. I calibrated the post-processing algorithm to the data format of the used preclinical MRI scanner. I conducted the *ex vivo* phantom studies and the simulation experiments for validation of EPI-MRE (see Figure 6,7a,8b). In the next phase, I analyzed the performance of EPI-MRE and the effect of SNR on algebraic Helmholtz inversion and tomoelastography (see Figure 7b). I found that tomoelastography resolves SWS values with greater accuracy than Helmholtz inversion. In the last phase, I demonstrated the feasibility of EPI-MRE with tomoelastography post-processing in several *in vivo* studies. Three studies [23, 24, 26] are summarized in the present dissertation and attached to the manuscript. In these studies, the MRI (MRE, DWI, ASL) was done entirely by me. I anesthetized the animals, prepared them for the experiments and measured them with the preclinical MRI scanner. I optimized the imaging parameters of MRE, DWI, and ASL for brain imaging, recorded the data set of MRE, DWI and ASL and reconstructed the elastograms, ADC maps and PRF maps in Matlab. Additionally, on the reconstructed images, I selected the ROIs of the analyzed brain regions in Matlab and derived the mean values for SWS, ADC and CBF in the analyzed sub-regions. I computed the group mean statistic for the MRE, DWI and ASL and created the figures. All figures in [23] and [24] are made by me. All figures related to MRE, DWI and T2* in [26] are made by me (Figure 1, Page 3; Figure 2a,b,c,d, Page 4; Figure 3, Page 4). With the exception of Figure 2, Figure 8a, Figure 17 and the MRS part of Figure 15, each figure presented in this dissertation is the result of my work and was made by me including the measurement and evaluation of the data for the figures. Additionally, I contributed to writing, editing and revising the published manuscripts.

8. References

1. Hirsch S, Braun J, Sack I. Magnetic Resonance Elastography - Physical Background and Medical Applications. Weinheim, Germany: Wiley-VCH; 2017.

2. Murphy MC, Curran GL, Glaser KJ, Rossman PJ, Huston J 3rd, Poduslo JF, Jack CR Jr, Felmlee JP, Ehman RL. Magnetic resonance elastography of the brain in a mouse model of Alzheimer's disease: initial results. *Magn Reson Imaging*. 2012 May;30(4):535-9.

3. Lipp A, Trbojevic R, Paul F, Fehlner A, Hirsch S, Scheel M, Noack C, Braun J, Sack I. Cerebral magnetic resonance elastography in supranuclear palsy and idiopathic Parkinson's disease. *Neuroimage Clin*. 2013 Sep 20;3:381-7.

4. Riek K, Millward JM, Hamann I, Mueller S, Pfueller CF, Paul F, Braun J, Infante-Duarte C, Sack I. Magnetic resonance elastography reveals altered brain viscoelasticity in experimental autoimmune encephalomyelitis. *Neuroimage Clin*. 2012 Sep 12;1(1):81-90.

5. Carney N, Totten AM, O'Reilly C, Ullman JS, Hawryluk GW, Bell MJ, Bratton SL, Chesnut R, Harris OA, Kissoon N, Rubiano AM, Shutter L, Tasker RC, Vavilala MS, Wilberger J, Wright DW, Ghajar J. Guidelines for the Management of Severe Traumatic Brain Injury, Fourth Edition. *Neurosurgery*. 2017 Jan 1;80(1):6-15.

6. Arani A, Murphy MC, Glaser KJ, Manduca A, Lake DS, Kruse SA, Jack CR Jr, Ehman RL, Huston J 3rd. Measuring the effects of aging and sex on regional brain stiffness with MR elastography in healthy older adults. *Neuroimage*. 2015 May 1;111:59-64.

7. Schregel K, Wuerfel E, Garteiser P, Gemeinhardt I, Prozorovski T, Aktas O, Merz H, Petersen D, Wuerfel J, Sinkus R. Demyelination reduces brain parenchymal stiffness quantified in vivo by magnetic resonance elastography. *Proc Natl Acad Sci U S A*. 2012 Apr 24;109(17):6650-5.

8. Jamin Y, Boult JKR, Li J, Popov S, Garteiser P, Ulloa JL, Cummings C, Box G, Eccles SA, Jones C, Waterton JC, Bamber JC, Sinkus R, Robinson SP. Exploring the biomechanical properties of brain malignancies and their pathologic determinants in vivo with magnetic resonance elastography. *Cancer Res*. 2015 Apr 1;75(7):1216-1224.

9. Pepin KM, Ehman RL, McGee KP. Magnetic resonance elastography (MRE) in cancer: Technique, analysis, and applications. *Prog Nucl Magn Reson Spectrosc*. 2015 Nov;90-91:32-48.

10. Bayly PV, Garbow JR. Pre-clinical MR elastography: Principles, techniques, and applications. *J Magn Reson*. 2018 Jun;291:73-83.

11. Bigot M, Chauveau F, Beuf O, Lambert SA. Magnetic Resonance Elastography of Rodent Brain. *Front Neurol*. 2018 Nov 27;9:1010.

12. Atay SM, Kroenke CD, Sabet A, Bayly PV. Measurement of the dynamic shear modulus of mouse brain tissue in vivo by magnetic resonance elastography. *J Biomech Eng*. 2008 Apr;130(2):021013.

13. Clayton EH, Garbow JR, Bayly PV. Frequency-dependent viscoelastic parameters of mouse brain tissue estimated by MR elastography. *Phys Med Biol*. 2011 Apr 21;56(8):2391-406.

14. Boulet T, Kelso ML, Othman SF. Long-term in vivo imaging of viscoelastic properties of the mouse brain after controlled cortical impact. *J Neurotrauma*. 2013 Sep 1;30(17):1512-20.

15. Klein C, Hain EG, Braun J, Riek K, Mueller S, Steiner B, Sack I. Enhanced adult neurogenesis increases brain stiffness: in vivo magnetic resonance elastography in a mouse model of dopamine depletion. *PLoS One*. 2014 Mar 25;9(3):e92582.

16. Liang Z-P, Lauterbur CP. Principles of Magnetic Resonance Imaging: A Signal Processing Perspective. Wiley-IEEE Press. 2000, ISBN: 9780780347236

17. Tzschatzsch H, Guo J, Dittmann F, Hirsch S, Barnhill E, Johrens K, Braun J, Sack I. Tomoelastography by multifrequency wave number recovery from time-harmonic propagating shear waves. *Med Image Anal* 2016;30:1-10.

18. Dietrich WD, Levi AD, Wang M, Green BA. Hypothermic treatment for acute spinal cord injury. *Neurotherapeutics*. 2011 Apr;8(2):229-39.

19. Yenari MA, Hemmen TM. Therapeutic hypothermia for brain ischemia: where have we come and where do we go? *Stroke*. 2010 Oct;41(10 Suppl):S72-4.

20. Jacobs SE, Berg M, Hunt R, Tarnow-Mordi WO, Inder TE, Davis PG. Cooling for newborns with hypoxic ischaemic encephalopathy. *Cochrane Database Syst Rev*. 2013 Jan 31;(1).

21. González-Ibarra FP, Varon J, López-Meza EG. Therapeutic hypothermia: critical review of the molecular mechanisms of action. *Front Neurol*. 2011 Feb 3;2:4.

22. Yenari MA, Onley D, Hedehus M, deCrespigny A, Sun GH, Moseley ME, Steinberg GK. Diffusion- and perfusion-weighted magnetic resonance imaging of focal cerebral ischemia and cortical spreading depression under conditions of mild hypothermia. *Brain Res*. 2000 Dec 8;885(2):208-19.

23. Bertalan G, Guo J, Tzschatzsch H, Klein C, Barnhill E, Sack I, Braun J. Fast tomoelastography of the mouse brain by multifrequency single-shot MR elastography. *Magn Reson Med*. 2019 Apr;81(4):2676-2687.

24. Bertalan G, Boehm-Sturmb P, Schreyer S, Morr A, Steiner B, Tzschätzsch H, Braun J, Guo J, Sack I. The influence of body temperature on tissue stiffness, blood perfusion, and water diffusion in the mouse brain. *Acta Biomater*. 2019 Sep 15;96:412-420.

25. Karanjia N, Geocadin RG. Post-cardiac arrest syndrome: update on brain injury management and prognostication. *Curr Treat Options Neurol*. 2011 Apr;13(2):191-203.

26. Bertalan G, Klein C, Schreyer S, Steiner B, Kreft B, Tzschätzsch H, de Schellenberger AA, Nieminen-Kelhä M, Braun J, Guo J, Sack I. Biomechanical properties of the hypoxic and dying brain quantified by magnetic resonance elastography. *Acta Biomater*. 2020 Jan 1;101:395-402.

27. Dong H, White RD, Kolipaka A. Advances and Future Direction of Magnetic Resonance Elastography. *Top Magn Reson Imaging*. 2018 Oct;27(5):363-384.

28. Muthupillai R, Lomas DJ, Rossman PJ, Greenleaf JF, Manduca A, Ehman RL. Magnetic resonance elastography by direct visualization of propagating acoustic strain waves. *Science*. 1995 Sep 29;269(5232):1854-7.

29. Klatt D, Johnson CL, Magin RL. Simultaneous, multidirectional acquisition of displacement fields in magnetic resonance elastography of the in vivo human brain. *J Magn Reson Imaging*. 2015 Aug;42(2):297-304.

30. Braun J, Guo J, Lützkendorf R, Stadler J, Papazoglou S, Hirsch S, Sack I, Bernarding J. High-resolution mechanical imaging of the human brain by three-dimensional multifrequency magnetic resonance elastography at 7T. *Neuroimage*. 2014 Apr 15;90:308-14.

31. Clayton EH, Garbow JR, Bayly PV. Frequency-dependent viscoelastic parameters of mouse brain tissue estimated by MR elastography. *Phys Med Biol*. 2011 Apr 21;56(8):2391-406.

31. Hain EG, Klein C, Munder T, Braun J, Riek K, Mueller S, Sack I, Steiner B. Dopaminergic Neurodegeneration in the Mouse Is Associated with Decrease of Viscoelasticity of Substantia Nigra Tissue. PLoS One. 2016 Aug 15;11(8).

32. Millward JM, Guo J, Berndt D, Braun J, Sack I, Infante-Duarte C. Tissue structure and inflammatory processes shape viscoelastic properties of the mouse brain. *NMR Biomed*. 2015 Jul;28(7):831-9.

33. Munder T, Pfeffer A, Schreyer S, Guo J, Braun J, Sack I, Steiner B, Klein C. MR elastography detection of early viscoelastic response of the murine hippocampus to amyloid beta accumulation and neuronal cell loss due to Alzheimer's disease. *J Magn Reson Imaging.* 2018;47(1):105-114.

34. Braun J, Tzschatzsch H, Korting C, Ariza de Schellenberger A, Jenderka M, Driessle T, Ledwig M, Sack I. A compact 0.5 T MR elastography device and its application for studying viscoelasticity changes in biological tissues during progressive formalin fixation. *Magn Reson Med*. 2018 Jan;79(1):470-478

35. Papazoglou S, Hamhaber U, Braun J, Sack I. Algebraic Helmholtz inversion in planar magnetic resonance elastography. *Phys Med Biol*. 2008 Jun 21;53(12):3147-58.

36. Arunachalam SP, Rossman PJ, Arani A, Lake DS, Glaser KJ, Trzasko JD, Manduca A, McGee KP, Ehman RL, Araoz PA. Quantitative 3D magnetic resonance elastography: Comparison with dynamic mechanical analysis. *Magn Reson Med*. 2017 Mar;77(3):1184-1192.

37. Mace E, Cohen I, Montaldo G, Miles R, Fink M, Tanter M. In vivo mapping of brain elasticity in small animals using shear wave imaging. *IEEE Trans Med Imaging*. 2011 Mar;30(3):550-8.

38. Christ AF, Franze K, Gautier H, Moshayedi P, Fawcett J, Franklin RJ, Karadottir RT, Guck J. Mechanical difference between white and gray matter in the rat cerebellum measured by scanning force microscopy. *J Biomech*. 2010 Nov 16;43(15):2986-92.

39. Hetzer S, Birr P, Fehlner A, Hirsch S, Dittmann F, Barnhill E, Braun J, Sack I. Perfusion alters stiffness of deep gray matter. *J Cereb Blood Flow Metab*. 2018 Jan;38(1):116-125.

40. Rungta RL, Choi HB, Tyson JR, Malik A, Dissing-Olesen L, Lin PJC, Cain SM, Cullis PR, Snutch TP, MacVicar BA. The cellular mechanisms of neuronal swelling underlying cytotoxic edema. *Cell*. 2015 Apr 23;161(3):610-621.

41. Plesnila N, Haberstok J, Peters J, Kölbl I, Baethmann A, Staub F. Effect of lactacidosis on cell volume and intracellular pH of astrocytes. *J Neurotrauma*. 1999 Sep;16(9):831-41.

Statutory Declaration

“I, Gergely Bertalan, by personally signing this document in lieu of an oath, hereby affirm that I prepared the submitted dissertation on the topic Quantitative tissue characterization by mechanical parameters in preclinical, small-animal models (Quantitative Gewebecharakterisierung mittels mechanischer Kenngrößen in präklinischen Kleintiermodellen), independently and without the support of third parties, and that I used no other sources and aids than those stated.

All parts which are based on the publications or presentations of other authors, either in letter or in spirit, are specified as such in accordance with the citing guidelines. The sections on methodology (in particular regarding practical work, laboratory regulations, statistical processing) and results (in particular regarding figures, charts and tables) are exclusively my responsibility.

Furthermore, I declare that I have correctly marked all of the data, the analyses, and the conclusions generated from data obtained in collaboration with other persons, and that I have correctly marked my own contribution and the contributions of other persons (cf. declaration of contribution). I have correctly marked all texts or parts of texts that were generated in collaboration with other persons.

My contributions to any publications to this dissertation correspond to those stated in the below joint declaration made together with the supervisor. All publications created within the scope of the dissertation comply with the guidelines of the ICMJE (International Committee of Medical Journal Editors; www.icmje.org) on authorship. In addition, I declare that I shall comply with the regulations of Charité – Universitätsmedizin Berlin on ensuring good scientific practice.

I declare that I have not yet submitted this dissertation in identical or similar form to another Faculty.

The significance of this statutory declaration and the consequences of a false statutory declaration under criminal law (Sections 156, 161 of the German Criminal Code) are known to me.”

Date Signature

Declaration of my own contribution to the publications

Gergely Bertalan contributed the following to the below listed publications:

Publication 1:

Bertalan G, Guo J, Tzschatzsch H, Klein C, Barnhill E, Sack I, Braun J. Fast tomoelastography of the mouse brain by multifrequency single-shot MR elastography. *Magn Reson Med* 81(4) (2019) 2676-2687.

Contribution:

The main focus of this publication was the development of the single-shot EPI-MRE sequence for preclinical mouse brain MRE. EPI-MRE, including sequence design, implementation and testing, was entirely developed by myself. I configured all hardware components and synchronized the used function generator and the MRI scanner. I programmed the imaging sequence in C++ programming language and equipped it with motion encoding gradients. I tested the sequence timing and I synchronized the sequence with the used function generator in order to avoid any latency between the motion encoding gradients and the external mechanical vibration. I calibrated the post-processing algorithm to the data format of the used preclinical MRI scanner. The development of EPI-MRE took approximately one year. In this publication, this new single-shot MRE technique was introduced to the MRE community and applied for in vivo mouse brain measurements.

I conducted the ex vivo phantom studies and the simulation experiments for validation of EPI-MRE. In the next phase, I analyzed the performance of EPI-MRE and the effect of signal-to-noise-ratio (SNR) on algebraic Helmholtz inversion and tomoelastography (k-MDEV inversion). I found that tomoelastography resolves SWS values with greater accuracy than Helmholtz inversion. In the last phase, I demonstrated the feasibility of EPI-MRE with tomoelastography post-processing in in vivo mouse brain MRE. I measured the stiffness of different regions of the mouse brain and could show that the stiffness varies greatly in different subregions of the brain.

Both the ex vivo and the in vivo measurements were performed by myself. I recorded and evaluated the entire data set of this publication alone and independently. The entire method and result section of the manuscript was written by me. Each figure presented in this publication is the result of my work and was made by me including the measurement and evaluation of the data for the figures. I contributed to the explanation of the biological background of the findings. I also contributed to writing, editing and revising the published manuscripts. Furthermore, I contributed to writing, editing and revising the published manuscript. The co-authors helped me with planning the in vivo measurements, handling the mice, explaining the biologically relevant findings and writing and revising the published manuscript. Dr. Tzschätzsch and Dr. Barnhill are the inventors of k-MDEV inversion and helped me to answer my critical questions during the adaptation of k-MDEV for mouse brain MRE.

Publication 2:

Bertalan G, Boehm-Sturm P, Schreyer S, Morr A, Steiner B, Tzschätzsch H, Braun J, Guo J, Sack I. The influence of body temperature on tissue stiffness, blood perfusion, and water diffusion in the mouse brain. *Acta Biomater*. 2019 Sep 15;96:412-420.

Contribution:

The design of this paper was done by me. During a test measurement I happened to notice that a difference of 1-2 °C in body temperature of the mice has a great influence on brain stiffness. Through my own literature research I became aware of therapeutic hypothermia, which is used in neuronal diseases, such as stroke, and leads to a better clinical outcome in patients. The new MRE method, which was established in the first publication (see publication 1), was used to study changes in brain stiffness that are caused by changes in body core temperature. For the first time, my developed MRE method enables a continuous monitoring of brain stiffness with a time resolution of 40 seconds due to its short measurement time.

I have applied MRE, diffusion weighted imaging (DWI) and perfusion weighted imaging (PRF) on seven mice in vivo. I cooled the body temperature of the mouse to 28 °C and slowly warmed it back to a normal temperature (38 °C). The warm-up process took 1.5 hour. During this rewarming, I continuously scanned the stiffness, diffusion and perfusion in the brain with a 7 Tesla Bruker MRI scanner. I correlated time resolved stiffness values with diffusion and perfusion in the brain and examined how these three parameters change in mouse brain in vivo by temperature modulation and in hypothermia.

I recorded and evaluated the entire data set of this publication alone and independently. The entire method and result section of the manuscript was written by me. Each figure presented in this publication is the result of my work and was made by me including the measurement and evaluation of the data for the figures. I contributed to the explanation of the biological background of the findings. I contributed to writing, editing and revising the published manuscript. The co-authors helped me with planning the in vivo measurements, handling the mice, explaining the biologically relevant findings and writing and revising the published manuscript.

Publication 3:

Bertalan G, Klein C, Schreyer S, Steiner B, Kreft B, Tzschätzsch H, de Schellenberger AA, Nieminen-Kelhä M, Braun J, Guo J, Sack I. Biomechanical properties of the hypoxic and dying brain quantified by magnetic resonance elastography. *Acta Biomaterialia* 81(4) (2019) 2676-2687.

Contribution:

I have contributed significantly to the production of this publication. The idea for this study was developed by my supervisor Prof. Sack and myself. The new MRE method, which was introduced in the first publication (see publication 1), was used to continuously monitor the changes in brain stiffness during the critical phase of death. EPI-MRE significantly reduced the measurement time for mouse brain

MRE. Short scan times in the order of only 40 seconds allowed, for the first time, continuous monitoring of stiffness during death.

Together with Dr. Guo, I have developed a hypoxic mouse model. In short, the mice received a lethal dose of ketamine, which led to a slow respiratory arrest and, about 5 minutes later, to cardiac arrest. During this period I continuously measured the stiffness and diffusion of the brain with a 7 Tesla Bruker MRI scanner. Dr. Nieminen-Kelhä opened a cranial window in three mice post mortem by a surgical procedure. I examined these mice again in the MRI scanner after the surgical procedure and continued the stiffness measurement. In this part of the study I examined the effect of a cranial window on stiffness changes.

I recorded and evaluated the entire MRE and DWI data set in this publication alone and independently.

Each figure presented in this publication on MRE and DWI (Figure 1, page 3; Figure 2a,b,c,d, page 4; Figure 3, page 4) is the result of my work and was made by me including the measurement and evaluation of the data for the figures. I contributed to the explanation of the biological background of the findings. I contributed to writing, editing and revising the published manuscript. The main finding of this publication, namely that a significant increase in stiffness occurs during the critical phase of dying, was exclusively due to my work. My EPI-MRE imaging sequence and my in vivo measurements allowed to determine this clinically relevant increase in stiffness during death.

_____

Signature, date and stamp of first supervising university professor / lecturer

_____

Signature of doctoral candidate

Publication 1: Tomoelastography of the mouse brain by multifrequency single-shot MR elastography

Journal Data Filtered By: **Selected JCR Year: 2016** Selected Editions: SCIE,SSCI
Selected Categories: "**RADIOLOGY, NUCLEAR MEDICINE and MEDICAL IMAGING**" Selected Category Scheme: WoS
Gesamtanzahl: 126 Journale

Rank	Full Journal Title	Total Cites	Journal Impact Factor	Eigenfactor Score
1	JACC-Cardiovascular Imaging	6,895	10.189	0.027050
2	RADIOLOGY	50,983	7.296	0.066140
3	EUROPEAN JOURNAL OF NUCLEAR MEDICINE AND MOLECULAR IMAGING	14,019	7.277	0.024910
4	Circulation-Cardiovascular Imaging	4,472	6.803	0.019120
5	JOURNAL OF NUCLEAR MEDICINE	24,977	6.646	0.037540
6	NEUROIMAGE	85,630	5.835	0.173210
7	JOURNAL OF CARDIOVASCULAR MAGNETIC RESONANCE	4,349	5.601	0.014950
8	SEMINARS IN RADIATION ONCOLOGY	2,232	5.356	0.003910
9	INVESTIGATIVE RADIOLOGY	5,925	5.195	0.011230
10	INTERNATIONAL JOURNAL OF RADIATION ONCOLOGY BIOLOGY PHYSICS	44,068	5.133	0.060060
11	ULTRASOUND IN OBSTETRICS & GYNECOLOGY	11,611	4.710	0.019350
12	HUMAN BRAIN MAPPING	18,139	4.530	0.041900
13	RADIOTHERAPY AND ONCOLOGY	15,639	4.328	0.028040
14	MEDICAL IMAGE ANALYSIS	5,539	4.188	0.010720
15	EUROPEAN RADIOLOGY	16,381	3.967	0.033340
16	IEEE TRANSACTIONS ON MEDICAL IMAGING	15,215	3.942	0.019660
17	JOURNAL OF NUCLEAR CARDIOLOGY	3,021	3.930	0.003920
18	MAGNETIC RESONANCE IN MEDICINE	29,816	3.924	0.035960
19	CLINICAL NUCLEAR MEDICINE	4,008	3.640	0.006470
20	SEMINARS IN NUCLEAR MEDICINE	2,056	3.630	0.002800
21	AMERICAN JOURNAL OF NEURORADIOLOGY	21,720	3.550	0.032180
22	MOLECULAR IMAGING AND BIOLOGY	2,228	3.466	0.005880
23	ULTRASCHALL IN DER MEDIZIN	1,907	3.452	0.003930
24	RADIOGRAPHICS	10,286	3.427	0.009660
25	Biomedical Optics Express	6,187	3.337	0.021610
26	Contrast Media & Molecular Imaging	1,131	3.307	0.002810
27	INTERNATIONAL JOURNAL OF HYPERTHERMIA	3,030	3.262	0.003810

https://doi.org/10.1002/mrm.27586

https://doi.org/10.1002/mrm.27586

https://doi.org/10.1002/mrm.27586

https://doi.org/10.1002/mrm.27586

https://doi.org/10.1002/mrm.27586

https://doi.org/10.1002/mrm.27586

https://doi.org/10.1002/mrm.27586

https://doi.org/10.1002/mrm.27586

https://doi.org/10.1002/mrm.27586

https://doi.org/10.1002/mrm.27586

https://doi.org/10.1002/mrm.27586

https://doi.org/10.1002/mrm.27586

Publication 2: The influence of body temperature on tissue stiffness, blood perfusion, and water diffusion in the mouse brain

Journal Data Filtered By: **Selected JCR Year: 2017** Selected Editions: SCIE,SSCI
Selected Categories: **"ENGINEERING, BIOMEDICAL"** Selected Category Scheme: WoS
Gesamtanzahl: 78 Journale

Rank	Full Journal Title	Total Cites	Journal Impact Factor	Eigenfactor Score
1	BIOMATERIALS	108,908	8.806	0.114670
2	Annual Review of Biomedical Engineering	4,653	8.788	0.006260
3	Biofabrication	2,758	6.838	0.005720
4	Acta Biomaterialia	30,640	6.383	0.049410
5	IEEE TRANSACTIONS ON MEDICAL IMAGING	17,837	6.131	0.024200
6	Advanced Healthcare Materials	6,465	5.609	0.019660
7	MEDICAL IMAGE ANALYSIS	6,383	5.356	0.011900
8	CLINICAL ORAL IMPLANTS RESEARCH	14,065	4.305	0.016880
9	IEEE TRANSACTIONS ON BIOMEDICAL ENGINEERING	21,496	4.288	0.023780
10	Journal of Tissue Engineering and Regenerative Medicine	3,963	4.089	0.006640
11	IEEE TRANSACTIONS ON NEURAL SYSTEMS AND REHABILITATION ENGINEERING	5,647	3.972	0.008260
12	Journal of Neural Engineering	5,551	3.920	0.009750
13	Journal of NeuroEngineering and Rehabilitation	4,325	3.865	0.009120
14	EUROPEAN CELLS & MATERIALS	3,115	3.667	0.004290
15	IEEE Transactions on Biomedical Circuits and Systems	2,543	3.500	0.005780
16	ANNALS OF BIOMEDICAL ENGINEERING	10,881	3.405	0.017170
17	JOURNAL OF BIOMEDICAL MATERIALS RESEARCH PART B-APPLIED BIOMATERIALS	8,513	3.373	0.008410
18	Journal of the Mechanical Behavior of Biomedical Materials	7,713	3.239	0.017270
19	JOURNAL OF BIOMEDICAL MATERIALS RESEARCH PART A	17,464	3.231	0.016510

https://doi.org/10.1016/j.actbio.2019.06.034

https://doi.org/10.1016/j.actbio.2019.06.034

https://doi.org/10.1016/j.actbio.2019.06.034

https://doi.org/10.1016/j.actbio.2019.06.034

https://doi.org/10.1016/j.actbio.2019.06.034

https://doi.org/10.1016/j.actbio.2019.06.034

https://doi.org/10.1016/j.actbio.2019.06.034

https://doi.org/10.1016/j.actbio.2019.06.034

https://doi.org/10.1016/j.actbio.2019.06.034

Publication 3: Biomechanical properties of the hypoxic and dying brain quantified by magnetic resonance elastography.

Journal Data Filtered By: **Selected JCR Year: 2018** Selected Editions: SCIE,SSCI
Selected Categories: "**ENGINEERING, BIOMEDICAL**" Selected Category Scheme: WoS
Gesamtanzahl: 80 Journale

Rank	Full Journal Title	Total Cites	Journal Impact Factor	Eigenfactor Score
1	Nature Biomedical Engineering	1,540	17.135	0.006440
2	Annual Review of Biomedical Engineering	4,634	12.257	0.004980
3	BIOMATERIALS	109,384	10.273	0.102160
4	MEDICAL IMAGE ANALYSIS	7,694	8.880	0.013370
5	IEEE TRANSACTIONS ON MEDICAL IMAGING	19,545	7.816	0.024990
6	Biofabrication	3,599	7.236	0.006680
7	Acta Biomaterialia	34,157	6.638	0.050150
8	Advanced Healthcare Materials	9,022	6.270	0.023290
9	Photoacoustics	512	5.250	0.001330
10	Journal of Neural Engineering	7,336	4.551	0.012190
11	IEEE TRANSACTIONS ON BIOMEDICAL ENGINEERING	23,794	4.491	0.021670
12	Artificial Cells Nanomedicine and Biotechnology	3,209	4.462	0.003030
13	IEEE Transactions on Biomedical Circuits and Systems	3,380	4.252	0.006910
14	CLINICAL ORAL IMPLANTS RESEARCH	13,819	3.825	0.015930
15	EUROPEAN CELLS & MATERIALS	3,184	3.682	0.003620
16	Journal of NeuroEngineering and Rehabilitation	4,974	3.582	0.008800
17	ARTIFICIAL INTELLIGENCE IN MEDICINE	2,462	3.574	0.002960
18	Journal of the Mechanical Behavior of Biomedical Materials	9,407	3.485	0.019210
19	IEEE TRANSACTIONS ON NEURAL SYSTEMS AND REHABILITATION ENGINEERING	6,548	3.478	0.008600

https://doi.org/10.1016/j.actbio.2019.11.011

https://doi.org/10.1016/j.actbio.2019.11.011

https://doi.org/10.1016/j.actbio.2019.11.011

https://doi.org/10.1016/j.actbio.2019.11.011

https://doi.org/10.1016/j.actbio.2019.11.011

https://doi.org/10.1016/j.actbio.2019.11.011

https://doi.org/10.1016/j.actbio.2019.11.011

https://doi.org/10.1016/j.actbio.2019.11.011

Curriculum Vitae

My curriculum vitae does not appear in the electronic version of my thesis for reasons of data protection.

My curriculum vitae does not appear in the electronic version of my thesis for reasons of data protection.

My curriculum vitae does not appear in the electronic version of my thesis for reasons of data protection.

My curriculum vitae does not appear in the electronic version of my thesis for reasons of data protection.

My curriculum vitae does not appear in the electronic version of my thesis for reasons of data protection.

List of publications

Bertalan G, Guo J, Tzschatzsch H, Klein C, Barnhill E, Sack I, Braun J. Fast tomoelastography of the mouse brain by multifrequency single-shot MR elastography. *Magn Reson Med.* 2019 Apr;81(4):2676-2687

Bertalan G, Boehm-Sturmb P, Schreyer S, Morr A, Steiner B, Tzschätzsch H, Braun J, Guo J, Sack I. The influence of body temperature on tissue stiffness, blood perfusion, and water diffusion in the mouse brain. *Acta Biomater*. 2019 Sep 15;96:412-420.

Bertalan G, Klein C, Schreyer S, Steiner B, Kreft B, Tzschätzsch H, de Schellenberger AA, Nieminen-Kelhä M, Braun J, Guo J, Sack I. Biomechanical properties of the hypoxic and dying brain quantified by magnetic resonance elastography. *Acta Biomater*. 2020 Jan 1;101:395-402.

Guo J, **Bertalan G**, Meierhofer D, Klein C, Schreyer S, Steiner B, Wangch S, Vieira da Silva R, Infante-Duarte C, Koch S, Boehm-Sturm P, Braun J, Sack I. Brain maturation is associated with increasing tissue stiffness and decreasing tissue fluidity. *Acta Biomater.* 2019 Nov;99:433-442

de Schellenberger AA, Tzschätzsch H, Polchlopek B, **Bertalan G**, Schrank F, Garczynska K, Janmey PA, Braun J, Sack I. Sensitivity of multifrequency magnetic resonance elastography and diffusion-weighted imaging to cellular and stromal integrity of liver tissue. *J Biomech.* 2019 May 9;88:201-208.

Acknowledgements

First, I would like to say thanks to my supervisors, especially Prof. Ingolf Sack and PhD Jürgen Braun for guiding me throughout the research work. Their knowledge, motivation and patience made my PhD project successful. Apart from the supervisors, I would like to say thanks to the rest of the team for the cooperative work. Finally, I am also grateful to my family, especially to my parents for the moral support, encouragement and motivation. I own a huge thanks also to my loving Marta who always understood and supported me during the last years when I had to stay longer at work.